Evidence from three-dimensional seismic tomography for a substantial accumulation of gas hydrate in a fluid-escape chimney in the Nyegga pockmark field, offshore Norway

Andreia Plaza-Faverola,[1,2] Graham K. Westbrook,[3] Stephan Ker,[1] Russell J. K. Exley,[3] Audrey Gailler,[3,4] Tim A. Minshull,[5] and Karine Broto[6]

[1] In recent years, it has become evident that features commonly called gas chimneys provide major routes for methane to pass through the methane-hydrate stability zone in continental margins and escape to the ocean. One of many such chimneys lying beneath pockmarks in the southeastern Vøring Plateau off Norway was investigated with a high-resolution seismic experiment employing a 2-D array of sixteen 4-component ocean bottom seismic recorders at approximately 100 m separation and a dense network of shots to define the 3-D variation of the chimney's structure and seismic properties. The tomographic model derived from *P* wave travel times shows that *P* wave velocity inside the chimney is up to 300 m/s higher than in the surrounding strata within the methane-hydrate stability zone. The zone of anomalously high velocity, about 500 m wide near its base, narrowing to about 200 m near the seabed, extends to a depth of 250 m below the seafloor. The depth extent of this zone and absence of high velocity beneath the base of the methane-hydrate stability field make it more likely that it contains hydrate rather than carbonate. If a predominantly fracture-filling model is appropriate for the formation of hydrate in low-permeability sediment, the maximum hydrate concentration in the chimney is estimated to be 14%–27% by total volume, depending on how host-sediment properties are affected by hydrate formation. Doming of the strata penetrated by the chimney appears to be associated with the emplacement of hydrate, accompanying the invasion of the gas hydrate stability zone by free gas.

Citation: Plaza-Faverola, A., G. K. Westbrook, S. Ker, R. J. K. Exley, A. Gailler, T. A. Minshull, and K. Broto (2010), Evidence from three-dimensional seismic tomography for a substantial accumulation of gas hydrate in a fluid-escape chimney in the Nyegga pockmark field, offshore Norway, *J. Geophys. Res.*, *115*, B08104, doi:10.1029/2009JB007078.

1. Introduction

[2] The escape of pore water and gas from continental shelves, through seafloor features known as pockmarks has been investigated for many years [*King and MacLean*, 1970]. The discovery of pockmarks in deeper water, within the gas hydrate stability field [e.g., *Vogt et al.*, 1994], led to a growing appreciation that the chimney-like features in the sedimentary strata beneath the pockmarks provide a means for methane beneath the hydrate stability zone to escape to the ocean, accompanied by the formation of gas hydrate [e.g.,

[1]Département Géosciences Marines, Ifremer, Plouzané, France.
[2]Department for Geology, University of Tromsø, Tromsø, Norway.
[3]School of Geography, Earth & Environmental Sciences, University of Birmingham, United Kingdom.
[4]Université Européenne de Bretagne, Brest, CNRS UMR 6538, Institut Universitaire Européen de la Mer, Plouzané, France.
[5]National Oceanography Centre, Southampton, United Kingdom.
[6]Institut Français du Pétrole, Rueil-Malmaison, France.

Riedel et al., 2006; *Chand et al.*, 2009; *Hustoft et al.*, 2009a]. The methane release through these chimneys in response to climate changes may be more significant than the methane released by submarine slides, which are commonly invoked as the mechanism for releasing methane from submarine hydrate [*McIver*, 1982; *Kvenvolden*, 2002].

[3] A pockmark field of about 2000 km[2] in the Nyegga region, north of the Storegga slide in the mid-Norwegian continental margin (Figure 1), where hydrate-related bottom-simulating reflectors commonly occur [*Mienert et al.*, 1998; *Bünz et al.*, 2003], contains hundreds of pockmarks underlain by chimney-like features, usually referred to as gas chimneys. In seismic reflection sections, chimneys are represented by zones of low coherence, scattering, and low amplitude that is, at least in part, a consequence of the seismic scattering in the shallowest parts of the chimneys. The surrounding strata appear truncated at the margins of the zone of incoherence and may also be flexed upward in the flanks of the chimney. Some of the truncation may only be apparent because of seismic visibility loss in the zone of incoherence, but in other cases, diffractions from points where strata meet the zone of incoherence show that truncation is real. In the uppermost
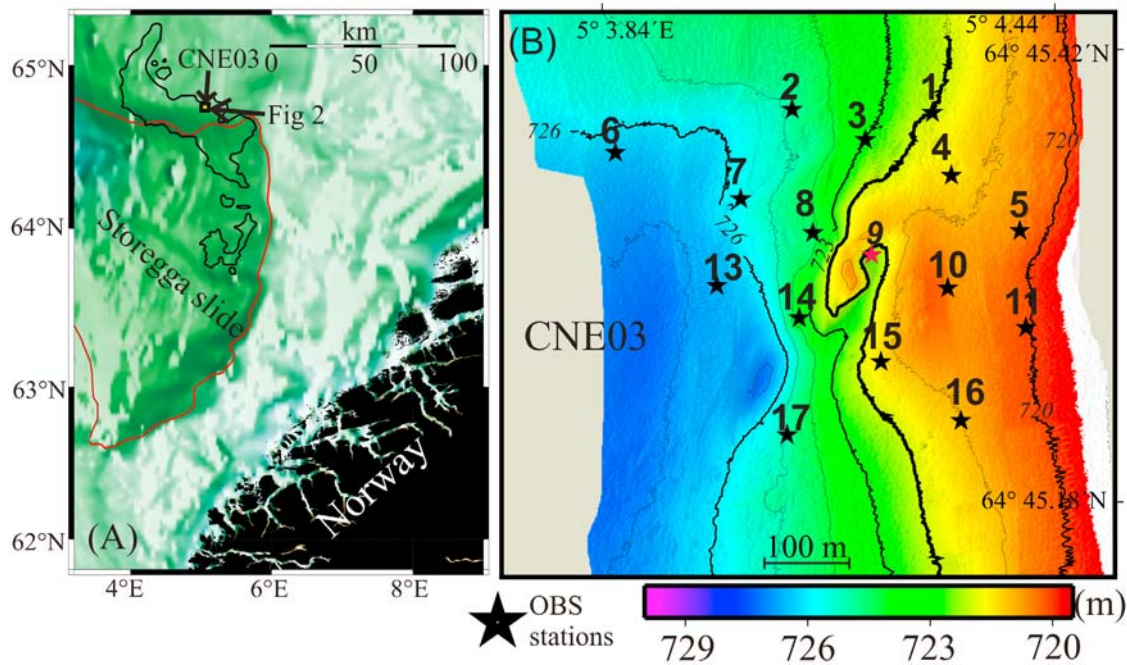
Figure 1. (a) Location and (b) bathymetry of the CNE03 pockmark at the mid-Norwegian continental margin. The CNE03 pockmark lies a few kilometers north from the Storegga slide (outlined in red in Figure 1a) and close to the northern limit of the prevalent BSR area (outlined in black in Figure 1a) [after *Bünz et al.*, 2003]. OBS sites are displayed around the pockmark. Only a limited amount of data from OBS 9 (at the center of the pockmark) was recovered.

200 m or so beneath the seabed, the chimneys (low-coherence zones) become wider with depth, and their width is typically greater than their depth. Deeper than the base of the gas hydrate stability zone (GHSZ), the chimneys may be under-lain by strata with very little disturbance or be shown to continue downward by the disturbance of the strata through which they pass. In many cases, however, the deeper part of the chimney is represented by a zone of very low amplitude incoherent reflections, which may be caused by amplitude loss in the upper part of the chimney producing a seismic shadow in the zone beneath. In some cases, the illusory nature of the apparent deeper continuation of chimneys has been demonstrated with seismic data with large shot-receiver offsets that can undershoot the scattering zone. The flux of methane through these features in the past is indicated by the occurrence in the pockmarks of methane-derived authigenic carbonate [*Hovland et al.*, 2005; *Mazzini et al.*, 2006] and shallow gas hydrate [*Ivanov et al.*, 2007], while variations in the depth beneath the seabed of the sulfate-methane transi-tion indicate different methane flux rates inside and outside pockmarks [*Paull et al.*, 2008].

[4] Flares of bubbles of methane in the water column have not been observed in the Nyegga area during the cruises, submarine dives, and remotely operated vehicle (ROV) operations carried out over the last 10 years. Hence, the chimneys at Nyegga are believed to be currently of very low activity or inactive in terms of the amount of free gas being released to the water column [*Hovland et al.*, 2005; *Hustoft et al.*, 2007; *Ivanov et al.*, 2007; *Paull et al.*, 2008]. However, seepage of dissolved methane has been observed at the G11 [*Hovland et al.*, 2005] and CNE03 pockmarks

[*Nouzé and Fabri*, 2007]. Also, the CNE03 pockmark was known from previous seismic imaging to exhibit significant local upwarping of reflectors that might be caused either by deformation related to fluid escape or by a seismic velocity anomaly caused by the presence of hydrate. As part of the HERMES (Hotspot Ecosystem Research on the Margins of European Seas) integrated project to study gas seeps sys-tems, a high-resolution seismic experiment was carried out in June 2006 to investigate the chimney-like features beneath the G11 [*Jose et al.*, 2008] and the CNE03 [*Westbrook et al.*, 2008b] pockmarks.

[5] In this paper we present the results of a detailed 3-D *P* wave reflection tomography study of the chimney beneath the CNE03 pockmark, using ocean bottom seismometer (OBS) data, which provides evidence for the occurrence of high-velocity material inside the chimney. The extent to which the interiors of the chimneys of the Nyegga-Storegga region are occupied by hydrate, carbonate or gas, as well as whether the internal strata suffered upward doming, had not been determined prior to the seismic investigation reported here. The results of the tomographic experiment constitute, therefore, a valuable contribution to the knowledge of the internal structure of chimneys in the Norwegian continental margin and to further understanding of their formation.

2. Geological Setting

[6] The chimney studied is one of the fluid-outflow fea-tures associated with pockmarks in the Nyegga pockmark field. The Nyegga region is located at around 64°N, 5°E. It lies above the Helland Hansen arch, which separates two

Table 1. Naust Formation's Stratigraphical Terminology, Unit Ages, and Lithology

Naust Units	*Rise et al.* [2006] Age (Ma)	*Berg et al.* [2005] Lithology
T	0–0.02	Glacial-marine with till and glacigenic debris flow
S	0.2–0.4	Glacial-marine to normal marine. Glacigenic debris.
U	0.4–0.6	Hard clays with variable sand and gravel Hemipelagic and glacial-marine at the base
A	0.6–1.5	Hemipelagic and remants from glacials
N	1.5–2.8	Glaciofluvial and marine processes

NE-SW trending Cretaceous basins: the Vøring to the northwest and the Møre basin to the southeast [*Brekke*, 2000]. Its eastern and western limits are the Trøndelag platform and the NW–SE trending Jan Mayen fracture zone respectively. The latest Cenozoic deposition was controlled by glacial and interglacial periods. The Plio-Pleistocene sedimentary wedge can be up to 1.75 km in thickness [*Hjelstuen et al.*, 1999]. The westward progression of the wedge and its fast deposition generated differential compaction in the underlying sediments, causing lateral fluid flow and fracturing of regions, depending on their position with respect to the front of the wedge [*Reemst et al.*, 1996; *Kjeldstad et al.*, 2003; *Gómez and Vergés*, 2005]. The sedimentation rate decreased in the Quaternary [*Hjelstuen et al.*, 1999].

[7] During Pleistocene glacial stages, thick sequences of glacigenic debris flows (GDFs) were deposited on the Norwegian continental shelf and slope. GDFs are composed of glacigenic material interfingered with very fine grained sediments [*Hjelstuen et al.*, 2005]. Along the Vøring margin, these glacigenic sequences are restricted to the uppermost continental slope [*Hjelstuen et al.*, 2005]. The CNE03 chimney-like feature, investigated here, is located far from the thick glacigenic sequences, which are mainly characteristic of the Naust units S and T [*Berg et al.*, 2005]. The lack of thick sequences of glacigenic debris flow is important because glacigenic debris flows are characterized by anomalous high seismic velocities.

[8] The sedimentary sequence containing the structures investigated with the seismic experiment lies within the Naust formation, for which we use the nomenclature and ages from *Rise et al.* [2006] (Table 1). Bottom to top, the units are named N, A, U, S, and T (0–2.8 Ma). Naust unit N (1.5–2.8 Ma) represents dominantly glaciofluvial and marine processes [*Rise et al.*, 2006]. Unit A (0.6–1.5 ma) represents a period where the ice sheets reached the paleo-shelf edge. It consists of hemipelagic sediments and remnants from land-based glaciers [*Berg et al.*, 2005].

[9] Sampled sediments from Naust-U (0.4–0.6 Ma) are predominantly hard clays with variable sand and gravel content [*Berg et al.*, 2005]. The shallower part of Naust-U is described as distal glacial marine together with hemipelagic deposition [*Berg et al.*, 2005]. According to borehole data, this upper sequence (Naust-U) has relatively high organic debris content and water content compared to the overlying strata [*Hustoft et al.*, 2007].

[10] Naust-S (0.2–0.4 Ma) represents predominantly glacial marine to normal marine conditions with glacial debris deposits on the slope [*Berg et al.*, 2005]. The transition from

U to S is characterized by a decrease of water content and plasticity. Naust-S lower sequences show more coarse-grained and unsorted sediments. However, the clay content increases again in the upper S sequence [*Berg et al.*, 2005].

[11] Finally, the top of Naust unit T (0–0.2 Ma) in the area of CNE03 is mainly glacial marine, with tills on the shelf and debris flow on the slope [*Berg et al.*, 2005]. Water content and clay content in the marine clay sediments within Naust are reported to be 30%–60% [*Bünz and Mienert*, 2004] and 50%–60%, respectively [*Berg et al.*, 2005].

[12] A gas hydrate-related bottom simulating reflector (BSR) has been mapped over an area of about 4000 km^2 of the gas hydrate province [*Bünz et al.*, 2003]. The BSR marks the transition between gas hydrate-bearing sediment above and sediments containing free gas below [*Bouriak et al.*, 2003; *Bünz et al.*, 2005; *Westbrook et al.*, 2008a]. The BSR is easier to see where the slope of the seabed causes the BSR to cut across the stratigraphy.

[13] Two major subbottom layers are inferred from P wave velocity (Vp) and seismic amplitude anomalies in Nyegga and its adjacent regions to be undercompacted and contain overpressured fluid [*Bünz et al.*, 2005; *Westbrook et al.*, 2008a; *Plaza-Faverola et al.*, 2010]. Hydraulic fracturing has been inferred to play a major role in the upward transportation of fluids in this region [*Berndt et al.*, 2003]. The Nyegga pockmark field in the eastern part of the mapped region of the BSR shows the highest density of seabed fluid venting to the north of the Storegga Slide [*Bouriak et al.*, 2000; *Bünz et al.*, 2003; *Hovland et al.*, 2005; *Hovland and Svensen*, 2006]. Some of the pockmarks have been described as complex structures with faunal communities and carbonate edifices associated with them [*Hovland et al.*, 2005; *Hovland and Svensen*, 2006; *Mazzini et al.*, 2006; *Paull et al.*, 2008].

[14] From the reported geothermal gradient in the region [*Sundvor et al.*, 2000; *Mienert et al.*, 2005], the variation in depth of the BSR with seabed depth 15 km to the southwest [*Bünz et al.*, 2003; *Westbrook et al.*, 2008a] and the measured seabed temperature at the location of CNE03 [*Nouzé and Fabri*, 2007], the depth of the present-day base of the GHSZ at CNE03 is predicted to be at about 230 m below the seafloor (mbsf) (Figure 9).

3. Experiment and Data

[15] The aim of the high-resolution seismic reflection tomography was to resolve the 3-D structure and variation of Vp in the chimney beneath the CNE03 pockmark. The tomographic experiment was part of an investigation that included data from a deep-towed 100 kHz side scan sonar and 5 kHz subbottom profiler. Both, single-channel seismic (SCS) and ocean bottom seismic (OBS) data were used in the tomographic inversion.

[16] An array of 16 OBSs was deployed around the pockmark (Figure 1) by lowering each OBS by cable, under guidance from acoustic navigation, to a height of 50 m above the seabed before releasing the OBS to fall to the seabed. This approach provided relatively precise positioning of the instruments in relation to the 300 m wide pockmark in a water depth of around 725 m [*Westbrook et al.*, 2008b]. Eight 4-component OBSs were recorded at a sampling interval of 0.4 ms. Eight 2-component OBSs were recorded at a 2 ms
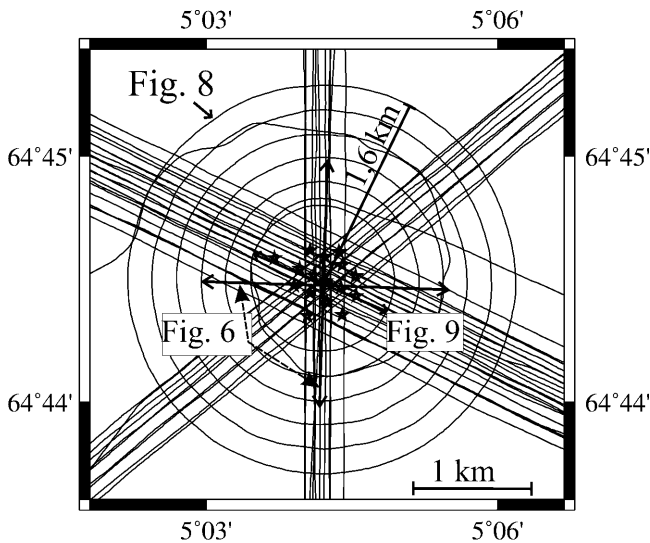
Figure 2. Geometry of the center of the seismic experiment, showing the seismic lines and OBS sites (stars), concentrated around the chimney.

sampling interval. The spacing of the OBSs was about 100 m. Only a small part of the data from one OBS located at the center of the pockmark could be recovered because of a fault with the recorder, and the data from this OBS were not used in the modeling. The seismic sources were mini-generator injector (GI) guns deployed as a single gun in true GI mode (configured as 13 cubic inch generator and 35 cubic inch injector) for recording part of the seismic lines set with a maximum resolution (shot spacing ~8 m; line spacing 50 m) and as two guns in harmonic mode to record lines with a better penetration (shot spacing ~12 m; line spacing 100 m). The seismic signal had a dominant frequency of 120 Hz.

[17] Single-channel seismic (SCS) reflection data were also recorded along the shot lines, including circles (Figure 2), which were designed to provide a good coverage of azimuths at farther offset ranges (Figures 2 and 3). Processing of the OBS data included a band-pass filtering (20–40–280–300 Hz.) to improve the data quality for picking. This filter removed the low frequency noise from the ship. Shots and OBSs were acoustically relocated using the direct wave travel times. The number of median residuals (between measured and predicted travel times) for each shot to all OBS out of the range −0.5 to +0.5 ms was negligible. At a shot-OBS offset of 500 m, a change in the expected direct wave travel time of 0.5 ms is produced by a change in range of 1.35 m [*Westbrook et al.*, 2008b].
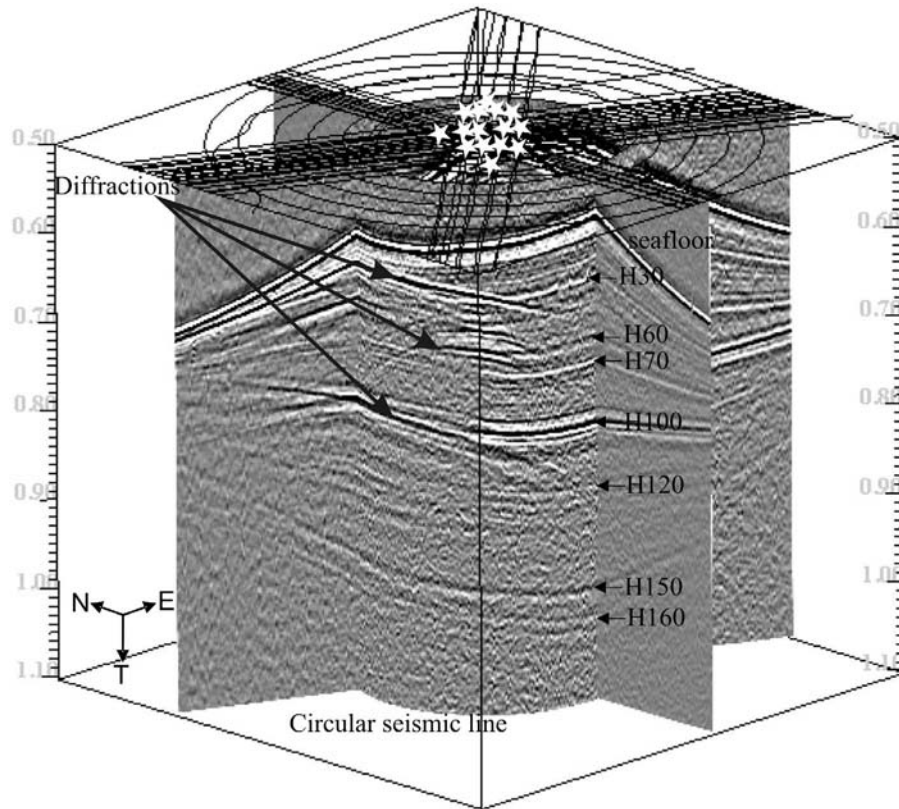

Figure 3. Selected seismic reflection sections from the OBS seismic experiment at the CNE03 pockmark showing the diffractions interfering with primary reflections. Arrivals from N–S, NW–SE, NE–SW, and circular seismic lines were recorded by an array of 15 OBSs (represented by stars). The seven seismic reflection events used for tomographic modeling are labeled.

[18] Detailed bathymetry of the CNE03 pockmark with a vertical resolution of 0.5 m, acquired by the ROV *Victor* [*Nouzé and Fabri*, 2007], provided visualization of the OBSs location with respect to the CNE03 pockmark morphology (Figure 1).

4. Modeling Methodology

4.1. *P* Wave Travel Time Picking

[19] *P* wave reflections were identified in 45 seismic lines recorded by 15 OBSs and a single-channel streamer. To ensure the same reflector was picked in all data sets, the SCS and OBS profiles were correlated (Figure 4). To facilitate the picking of travel times, the reflectors in the record sections were flattened or had their curvature reduced by applying a hyperbolic-move-out correction. The maximum offset range for picked arrivals was 2 km. Automatic and semiautomatic picking could be implemented, but spurious irregular time picks needed to be corrected manually. By visual inspection, 1 and 2 ms were set as errors in picking the data sampled at 0.4 and 2 ms, respectively. We have therefore considered 2 ms as a maximum data uncertainty (1/5 of the dominant period of the signal).

[20] Seven seismic reflectors were interpreted and correlated with the published stratigraphy of the region [*Rise et al.*, 2006; *Hustoft et al.*, 2007]: reflector H30 corresponds to intra Naust T (Figure 4). Horizons H60 and H70 are within Naust S. H100 is at the transition of Naust S and Naust U. This reflector is characterized by strong amplitudes and reverse polarity in most of the seismic sections. It is complicated by triplications and diffractions from the flanks of the chimney (Figures 3 and 4). H120 is the base of a low-velocity layer within Naust U [*Bünz et al.*, 2005; *Westbrook et al.*, 2008a]. H150 and H160 are the top and base, respectively, of a layer correlated with a layer within Naust unit A that is interpreted to be overpressured [*Reemst et al.*, 1996; *Bünz et al.*, 2005].

[21] To enhance deeper reflectors (below the base of GHSZ), a technique consisting of the summation of the hydrophone and vertical component of the geophone (PZ summation) was implemented. This technique enhances the amplitude of the upgoing waves containing the reflected arrivals and suppresses the amplitudes of the downgoing waves containing noise primarily. Events H120, H150, and H160 were picked from the PZ-summed profiles.

[22] Picking travel times of *P* waves reflections toward the N-E of the chimney above the base of the GHSZ was complicated by the presence of diffracted events and by seismic attenuation. Picking reflector H120 (right below the base of GHSZ) was mainly affected by blanking inside the chimney. Picking the deepest two reflectors was only limited by the blanking inside the chimney. Travel times of rays crossing the chimney were included in the tomography. These travel times helped constrain velocities in zones where the density of seismic-ray impact points was poor (e.g., at the flanks and chimney interior).

4.2. Inversion and Parameterization

[23] To build the velocity model, we used TomoInv, prestack travel time tomography software developed at Institut Français du Pétrole (IFP) and industrialized in a partnership between IFP and Parallel Geosciences Corporation (PGC).

Travel time tomography aims to determine the subsurface velocity model that best satisfies the travel times of seismic waves that propagate through the subsurface (Appendix A).

4.2.1. Velocity Distribution Representation

[24] The tomographic model uses a blocky representation for the velocity distribution. The model is divided into blocks with smoothly varying interface depths and velocity controlled by B-spline functions (Figure B3) (Appendix B) to ensure the continuity of derivatives with respect to the model up to second order [*Clarke*, 1996]. The tops and bases of the blocks correspond to seismic reflectors (seven in our study, Figure 4) that were chosen as the boundaries of the layers in the model (six in our study). Since each velocity block is characterized by its own smooth velocity distribution, the blocky representation provides the possibility of properly modeling discontinuous velocity variations and hence discontinuous travel times after ray tracing [*Lailly and Sinoquet*, 1996]. For the tomographic model of the CNE03 chimney, the velocity within a single layer remained vertically invariant.

4.2.2. Ray Tracing

[25] Ray tracing is performed by the bending method [e.g., *Jurado et al.*, 1996]. This method has advantages in term of its speed and offers a sufficient accuracy compared with other ray tracing methods [*Jurado et al.*, 1996]. An initial raypath linking source and receiver and obeying the Snell-Descartes law at each intersection between the trajectory interfaces and the reflector (impact points) is estimated. A raypath is retrieved by moving the impact point along the reflector until the initial trajectory satisfies the Fermat principle, i.e., the time function is stationary (Figure 5). The total time from source and receiver is then the ray travel time [*Jurado et al.*, 1996].

4.2.3. Regularization

[26] The tomographic inversion is an iterative process. The current velocity model is updated in order to minimize the misfits between observed and calculated travel times (equation A3, Appendix A). One major difficulty encountered when trying to solve the tomographic problem is that the solution, although providing the best match between observed and computed travel times, does not necessarily yield a model that is probable on the basis of geological and other geophysical information, often because errors in the data generate spurious small-scale details in the model. The progress of the inversion towards the optimum global solution (minimizing residual times, $T_{calculated} - T_{observed}$) can be halted by becoming trapped in local minima, especially when the starting model is far from the real geology (expected final model).

[27] To reduce this underdetermination, a dedicated approach based on the introduction, through regularization, of a priori information about the model (more precisely on its roughness), as well as a quasi-automatic management of the resulting regularization weights was employed. Hence, the tomographic algorithm provides control of the roughness and variability of expected surfaces and velocities by means of regularization weights. In particular, with this approach, one can find progressively less and less smooth models as the calculated travel times get closer to the observed travel times (Appendix A). In addition to the regularization, constraints can be placed on the model, such as an a priori range of velocity values or interface depths obtained from well
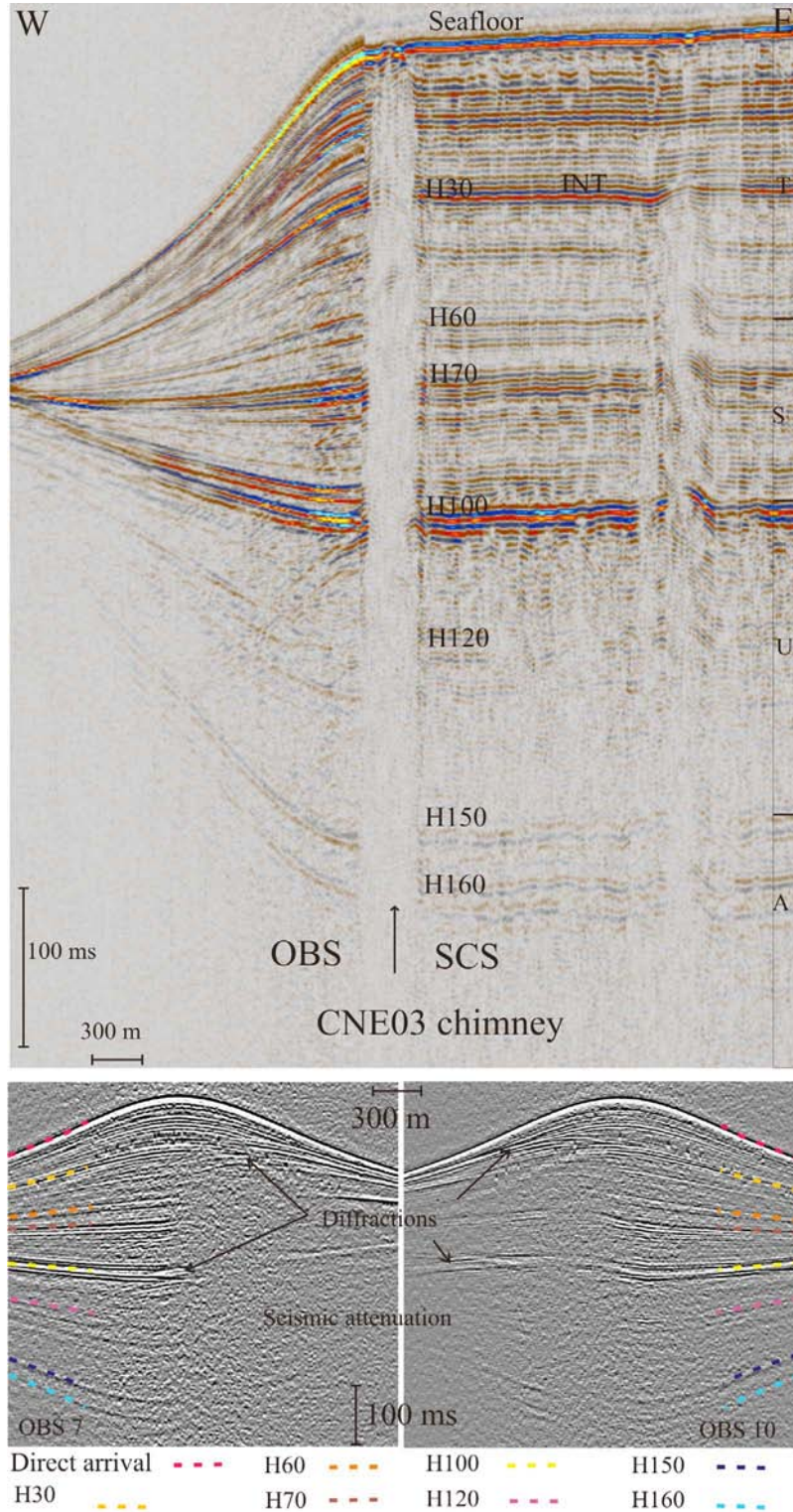
Figure 4. (top) Correlation between the OBS and streamer data. The interpreted reflectors have been correlated with the published seismic stratigraphy of the area [*Rise et al.*, 2006]. (bottom) OBSs 7 and 10 profiles recording from the western and eastern flanks of the chimney, respectively, show the seismic attenuation and diffractions impeding picking of the main reflectors at both sides of the chimney. The interpreted reflectors are indicated (dashed lines).
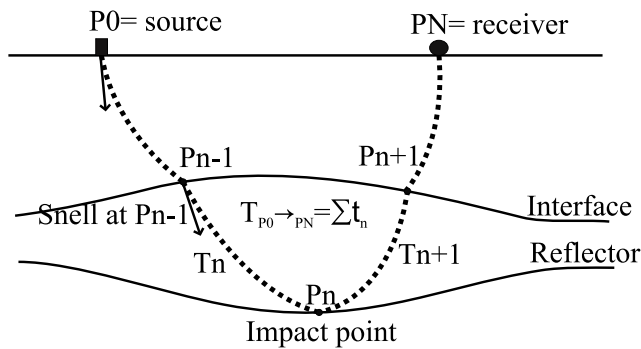
Figure 5. Schematic representation of the ray tracing, modified from *Jurado et al.* [1996].

data, forward modeling, or any other kind of velocity data available in the area [*Delbos et al.*, 2006]. Information on the resolution of the tomographic model of the CNE03 chimney can be found in Appendix B.

[28] The effectiveness of the tomography software and the methodology presented here have been demonstrated on several real data sets and in different geological contexts such as subsalt imaging, subchalk imaging with P wave reflections and P-to-S converted waves and vertical transverse isotropic symmetry anisotropy estimation, and foothills imaging [e.g., *Ehinger et al.*, 2001, *Broto et al.*, 2003, *Jardin et al.*, 2006].

4.2.4. Parameterization

[29] The 3-D tomographic model for CNE03 has dimensions $4 \times 4 \times 1.4$ km in *x*, *y*, and *z*, respectively. The cell size is 40×40 m in *x* and *y* (100 × 100 per layer). The cell size was chosen taking into account the shot spacing (~12 m). During the course of the inversions, the sensitivity of the calculated velocities to cell size was investigated with checkerboard tests (Appendix B). Seven major reflectors within

the upper 500 mbsf were included in the model. The first layer in our model is the water column. The seafloor interface and water velocity were not derived by tomographic inversion. The seafloor interface was derived by the depth conversion of the seafloor reflector map in the SCS, using the average velocity of the water column, 1.475 km/s, which was derived from inversion of the direct wave travel times during acoustic relocation of the OBSs [*Westbrook et al.*, 2008b]. Flat interfaces were used to initialize the inversion of all the layers. Initial velocities were taken from 1-D and 2-D models from previous studies a few tens of kilometers south [*Plaza-Faverola et al.*, 2010] and south-west [*Bünz et al.*, 2005; *Westbrook et al.*, 2008a] from CNE03. Details of the analysis of the residuals and model uncertainty are presented in Appendix B.

5. Results

5.1. Vp Model at CNE03

[30] The subseafloor layers in the model will be referred to, from shallow to deep, as L30, L60, L70, L100, L120, L150, and L160.

[31] Considerable differences exist between the lateral variation of Vp in layers above the base of the GHSZ (~230 mbsf) and in layers below it (Figure 6). The upper 230 m of sediments exhibit lateral velocity changes, with Vp increasing toward the chimney center. In some cases the Vp increases coincide with doming of the upper interfaces of the layers (Figures 6 and 7). In contrast, the layers underlying the GHSZ do not show large lateral changes in velocity.

[32] Although the travel times of rays with offsets (source-receiver horizontal distance) of up to 2 km were included in the inversion, the zone in which crossing rays occur is controlled by the positions of the OBS and by the depths of the reflecting interfaces. The large thickness of the water layer in comparison with the subseabed depths of
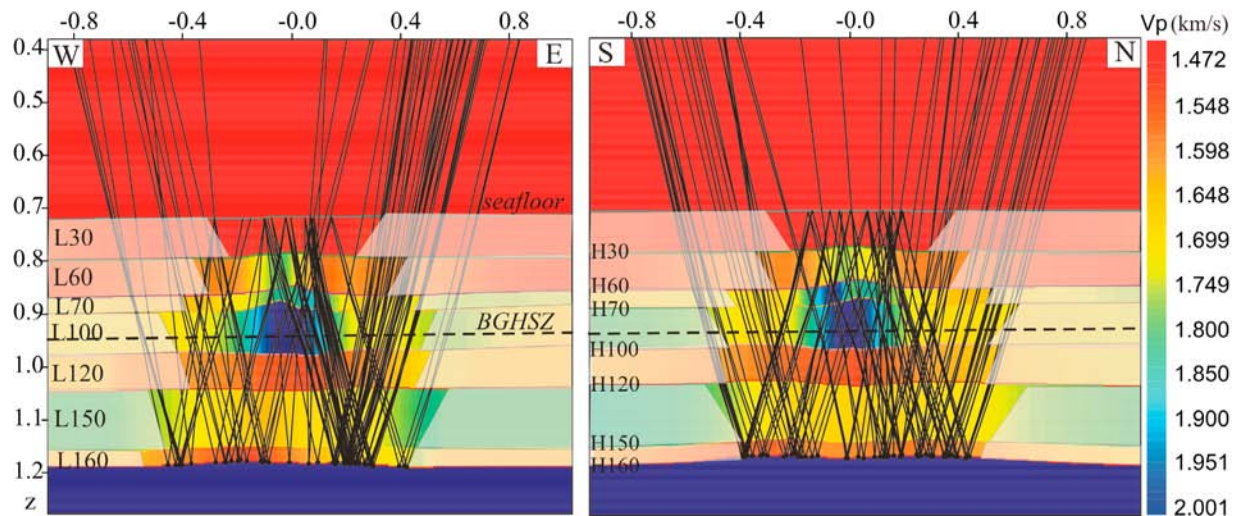

Figure 6. Velocity distribution in the E–W and N–S directions. See location in Figure 2. Each section is labeled with the identifiers of the interpreted layers. Vertical and horizontal scales are in kilometers. Vp is in kilometers per second. A cluster of raypaths is displayed to show the extent of the zones with well-constrained velocity in the model. For display purposes, the number of rays is decimated by a factor of 100. Velocities in the pale colored zones are undetermined by the inversion. The dashed black line corresponds to the calculated base of the GHSZ.
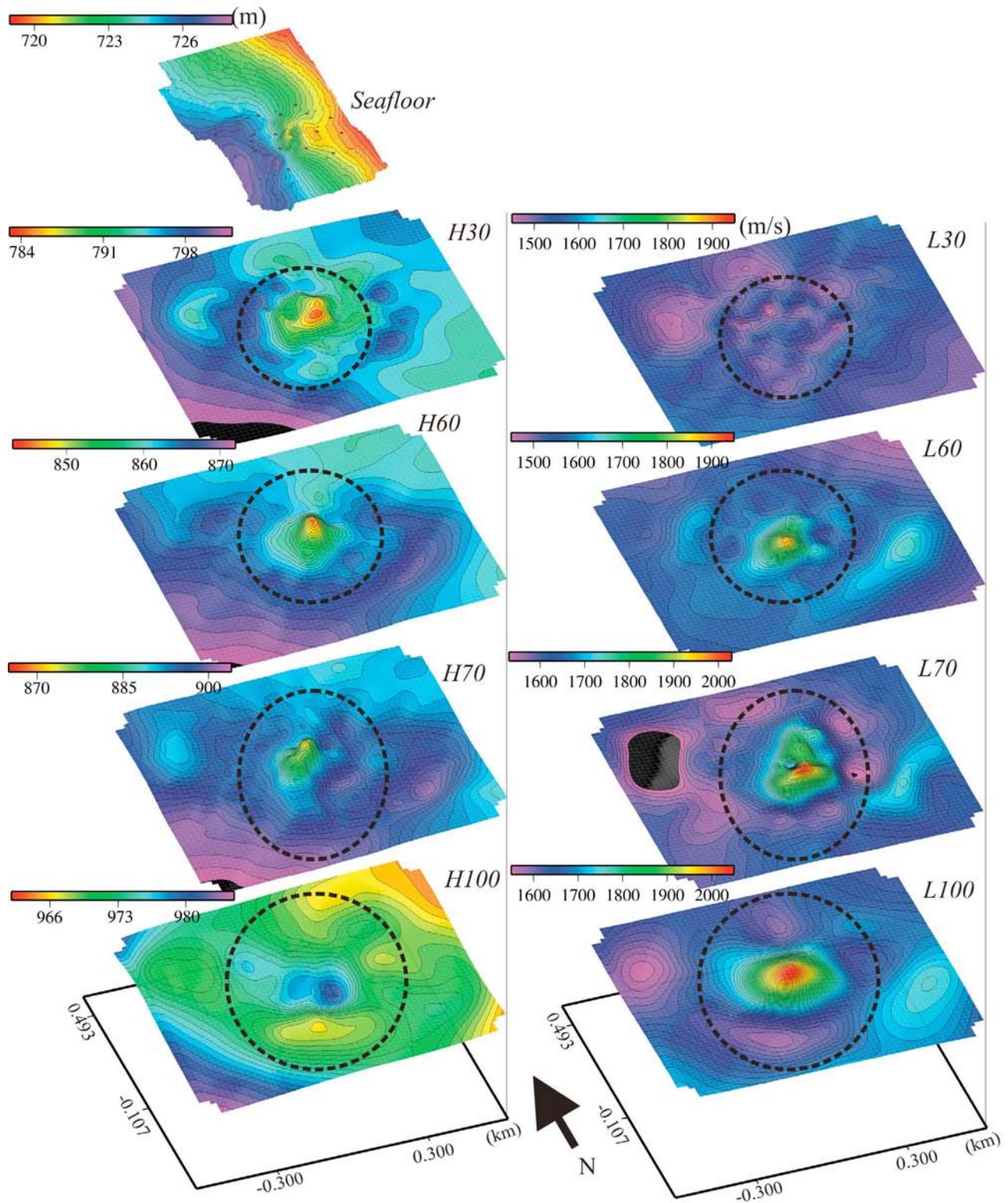
Figure 7. (left) Top view of the modeled interfaces depths and (right) velocities for layers above each interface focusing on their relief and anomalous lateral Vp changes within the GHSZ (H30, H60, H70, and H100). The color scales representing depth and velocity are different for each layer (the color scale is normalized to the maximum and minimum values). Contours are at 1 m intervals for depth and 10 m/s intervals for velocity. The dashed lines encircle the well-constrained regions for each modeled layer. The three upper layers are characterized by doming of their basal surfaces.

the reflectors place the impact points much closer to the OBS than to the shots. The radius of the zone in which crossing rays occur increases with depth from about 350 m for layer L30 to about 800 m for layer L160. Outside this radius, the low density or absence of rays toward the borders of the model leads to poor constraints of interface and velocities (border effect), resulting in an inaccurate Vp estimate. The border effect is minimal inside this radius, and a high concentration of observed travel times provides robust results for this region.

[33] Layer thicknesses in the model vary between 30 and 100 m (Figure 6). The shallowest reflector used in the model (base of L30, intra Naust T) is located at 80 mbsf (Figure 6). The interface is characterized by a gentle relief. Velocities in L30 need care in interpretation, because, although the velocity beneath the pockmark in the model is about 40 m/s greater than background, the impact points on the reflectors at its base (H30) cluster closely around each OBS, and so velocity is patchily defined in the layer.

[34] Positive relief of the second and third subseabed interfaces follows a NE–SW trend. Here, the magnitude of the relief of the model increases with depth (Figure 7). The maximum relief (measured respect to the flat part of the reflectors) is approximately 14 m at H30 and 22 m at H70. At H60 the relief coincides with a velocity increase toward the center of the chimney from 1580 up to 1880 m/s (Figure 7). The velocity increase is larger at the depth of H70. Vp outside the chimney is 1650 m/s on average, and it is up to 2000 m/s at the interior. For L70, the pattern of anomalously high velocity does not correlate so closely with the morphology of the base of the layer (e.g., the location of maximum Vp does not coincide with the location of maximum interface relief) as it does for the layers above (Figure 7).

[35] Layer L100 has a similar velocity distribution to L70, with an increased Vp of up to 2000 m/s inside the chimney. The basal reflector of L100 is 20 m deeper than the theoretical base of the GHSZ (see section 6). The appearance of high Vp beneath the base of the GHSZ (Figure 6) is, therefore, related to the choice of the L100 basal interface for inversion. Excluding this possibly hydrate-free zone (beneath the calculated base of the GHSZ) from the L100 layer inversion would probably lead to higher predicted anomalous velocities in the overlying layer (most of L100). Modeling was not attempted, however, for lack of a well-defined reflector above H100 close to the top of the potentially hydrate-free zone and because of the thinness of that zone.

[36] The basal interface of L100 has a gentle concave shape that reaches a maximum depression of -10 m with respect to the flat sediments towards the south-east of the chimney interior (Figure 7). Modeling of this interface is not optimal because impact points cover only half the area of the central depressed part of the base (see Figure B1, Appendix B). Consequently, the concave shape of the interface may, in part, result from a velocity-depth trade-off. The thickness of this layer (80–100 m) and wide range of incidence angles makes it less prone to this trade-off. If, however, the trade-off were enough to depress a truly flat base, the true maximum velocity of L100 would be 1800 m/s.

[37] Below the GHSZ, a 50 m thick layer (L120) shows velocities of less than 1550 m/s (Figure 6). A 100 m thick layer (L150) with a nearly flat base, and homogenous lateral distribution of Vp separates L120 from L160, a second low-velocity zone (LVZ) (Figure 6). The velocity of this second LVZ is not well determined, as it is a thin layer of about 30 m thickness at a depth of 470 mbsf. Both LVZs, however, can be correlated with high-amplitude negative-polarity reflections at their tops and with the two LVZs found within adjacent parts of the Nyegga area during previous studies [*Bünz et al.*, 2005; *Westbrook et al.*, 2008a; *Plaza-Faverola et al.*, 2010].

5.2. Correlation Between Seismic Anomalies and the Lateral Extent of the L70 High-Velocity Zone

[38] To qualitatively evaluate the nature of the chimney boundaries in the tomographic model, we correlated the extent of the anomalously high-velocity zone (HVZ) in layer L70 in the model with the seismic character of rays reflected from the base of L70 that crossed the area of the chimney from different azimuths. For this approach, we implemented a simple methodology that consisted of tracing rays in a 2-D plane linking the OBS sites to shots along the circular shot lines from which the seismic records showed evidence of lateral discontinuity, such as the origins of scattered waves, truncated reflectors, and the onset of distinct velocity pull-up, to form a polygon circumscribed by the rays that had grazed the margins of the chimney. The polygon was projected on the Vp map for L70 layer (Figure 8).

[39] The area enclosed by crossing polygons corresponds to the anomalous HVZ (Figure 8e). Scattering of the waves crossing the chimney makes it difficult to recognize the velocity pull-ups at some locations, e.g., at the western flank of the chimney (Figures 8a and 8d). However, at other locations and for some azimuths (e.g., at the eastern flank when the waves cross the structure in a NE–SW direction), the velocity pull-up can be recognized in spite of the seismic attenuation (Figure 8d, left of D3). The diffractions recorded at the flanks and front of the chimney (e.g., the phase reversal diffraction SD in Figure 8) also show differences related to the azimuth of the trajectory of the waves passing through the velocity anomaly inside the chimney (Figures 8a, 8b, 8c, and 8d). In the seismic profiles recorded by OBSs 1 and 17, recording from the NE and SW flanks, respectively, the shallowest diffraction at the top of the chimney (SD) dips to the east (Figures 8b and 8d). This same shallow diffraction (SD) is symmetrical with respect to the center of the chimney in OBSs 6 and 11 (recording from WNW and ESE, respectively) (Figures 8a and 8c). The observed azimuth-related differences indicate that the material inside the chimney that causes seismic scattering is heterogeneously distributed.

6. Discussion

6.1. Internal Structure of the Chimney

[40] The tomographic model's interfaces above H100 dome upward beneath the pockmark (Figure 7). This is also shown by the seismic sections after migration and depth conversion using the velocity field of the model (Figure 9). The seabed is domed upward around the central depression of the pockmark. The geometry of the shallowest (<10 mbsf) layers seen in the deep-towed, subbottom profiler records across the pockmark [*Westbrook et al.*, 2008b] shows that the amplitude of the dome after correction for the central depression is about 11 m. The amplitudes of the dome for
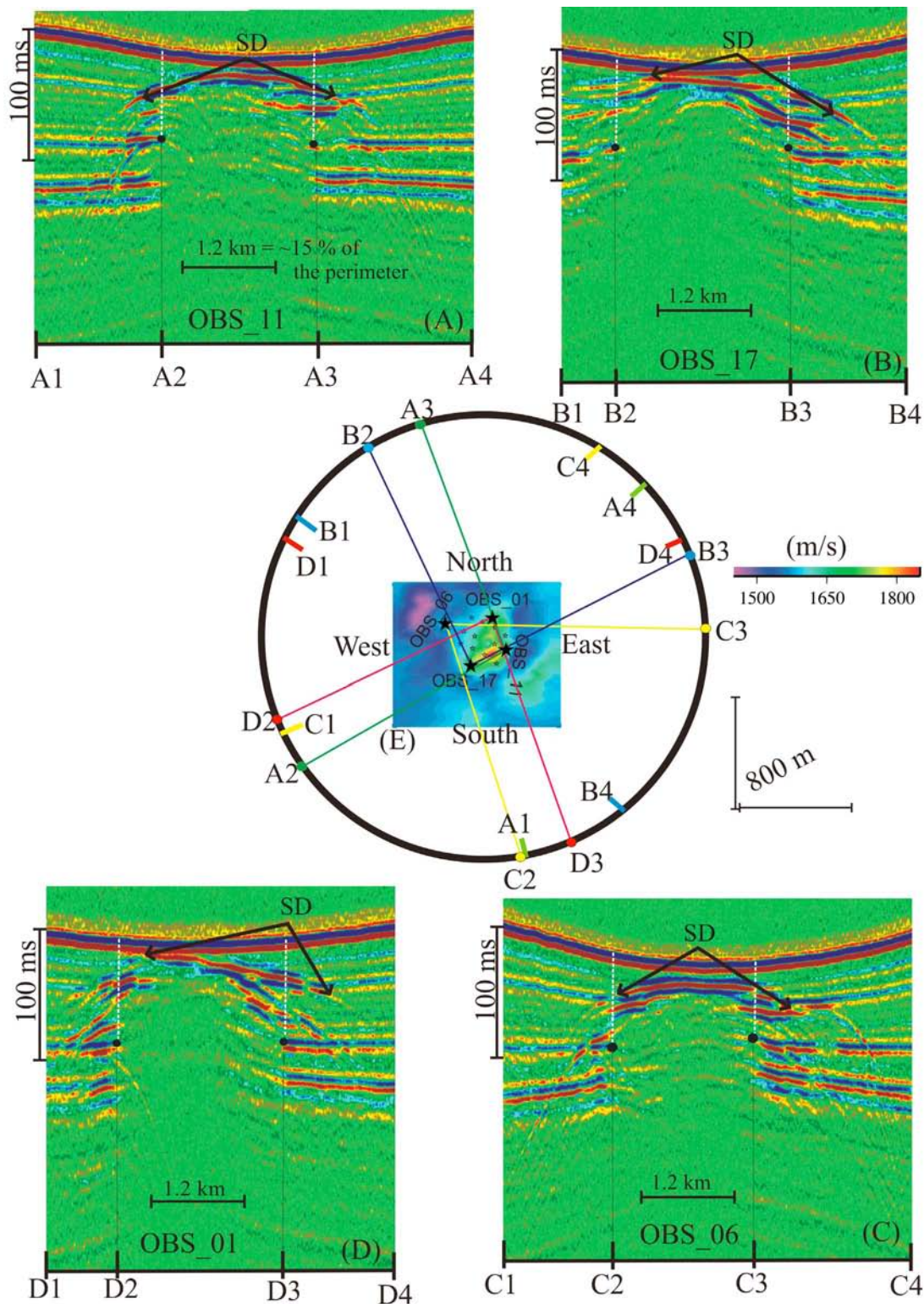
Figure 8. Seismic sections recorded by OBSs (a) 11, (b) 1, (c) 6, and (d) 17 from the outermost circular shot line (Figure 2). The sections show the width of the region of attenuation inside the chimney and travel time thinning (pull-up) of the reflectors. Lines linking the OBS sites with beginning and end of the region of attenuation (thick black dots) are plotted inside the circular seismic line over the (e) top view of H70 Vp. The length of the seismic record sections shown in Figures 8a, 8b, 8c, and 8d is indicated in the circle in Figure 8e by the corresponding labels in the seismic sections. A major diffraction at the front of the chimney is indicated by SD, and it is compared in the four OBS seismic sections (Figures 8a, 8b, 8c, and 8d).
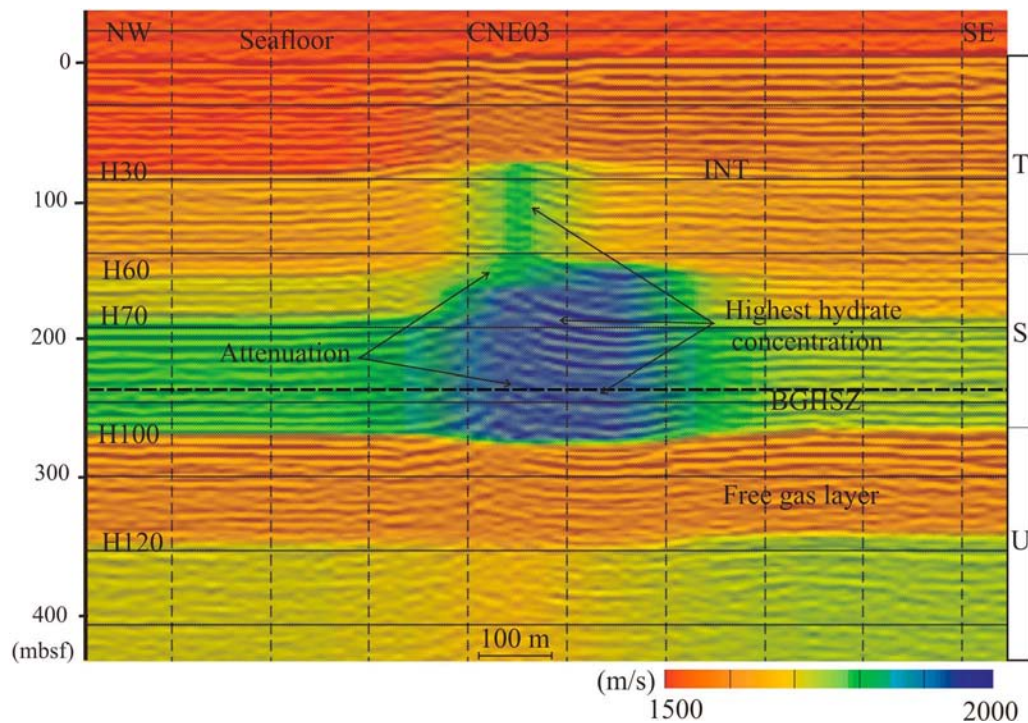
Figure 9. Inferred CNE03 chimney structure presented on a NW–SE oriented seismic reflection section (see Figure 2 for location) on which the Vp model has been overlain. The seismic attenuation is stronger at the western half of the chimney. The structural relief of reflectors increases only very slightly toward the base gas hydrate stability zone (BGHSZ).

interfaces (Figures 6 and 7) H30, H60, and H70 in the model are 14, 19, and 22 m, respectively. The amplitudes shown by the seismic reflectors H30, H60, and H70 on the depth section (Figure 9) are 23, 23, and 22 m, respectively. The correspondence between the model and the reflectors is good for H60 and H70 but not for H30. The probable reason for the difference is that the H30 interface in the model has no ray impact points in the center of the dome (Figure B1), and because of the smoothness imposed by regularization in the inversion, the model underestimates the curvature of the H30 surface. Consequently, it appears that the amplitude of the dome is about the same from H70 to H30 but is only half as high at the seabed. With the exception of L100, the layers hardly change thickness across the dome or, in the case of L30, thin slightly. This is additional verification that the velocity changes within these layers are not a consequence of a trade-off between velocity and thickness in the modeling.

[41] Layer L100 is thickened in the chimney. The base of the modeled layer (H100) lies at the top of a low-permeability unit above what is inferred to be a high-porosity unit containing free gas, because of its low velocity. In the region around the chimney, the H100 reflector is clearly stratigraphic in origin and displays no bottom-simulating characteristics. The predicted base of the GHSZ lies about 20 m above the H100 reflector. With no appreciable gas content in the low-permeability unit, the base of the GHSZ does not exhibit a BSR. The probable absence of hydrate in the bottom 20 m of layer L100 will dilute the effect of hydrate in the rest of L100 on the L100 velocity, which is vertically invariant for each cell of the model. The variation in velocity within L100 shows some correlation with the depth of its

base (Figure 7), and so one cannot exclude the possibility that for L100 there is some trade-off between velocity and thickness in the inversion, but particularly when one takes into account the probable absence of hydrate in the bottom 20 m of L100, the magnitude of the lateral variation of velocity within L100 is too large to be explained solely by a trade-off between velocity and thickness.

[42] Beneath the chimney, one would expect the basal part of L100, below the GHSZ, to be invaded by gas in fractures, locally reducing its velocity. The increase in travel time caused by this region of gas invasion could be modeled as a thickening of the layer and may be the cause of the slight deepening of the lower boundary of L100 beneath the chimney. Also, if warm fluids continue to carry heat upward through the base of the chimney, the increased temperature will move the base of the GHSZ locally higher, increasing the low velocity volume that occupies the bottom part of L100. It must be admitted that the detail of the chimney base in L100 is poorly resolved by the seismic data and that interpretation of this part of the tomographic model should be approached with caution.

[43] Beneath H100, the boundaries exhibit no doming (Figures 6 and 9), an observation confirmed by an image of the chimney in an industry seismic section from data with source-receiver offsets of up to 2400 m. This implies that whatever the process responsible for the doming of the chimney, it occurs within the GHSZ or at its immediate base.

[44] It is an interesting question as to whether there is any free gas in the chimney at present. Seismic blanking and scattering, however, coincide with structural disturbance and anomalously high Vp (Figure 8). Differences in areas affected

Table 2. Results of the Estimation of Hydrate Concentration for Two Cases[a]

Layer	Maximum Velocity (km/s)	Hydrate Velocity (km/s)	Minimum. Background Velocity (km/s)	Maximum Background Velocity (km/s)
L60	1.800	3.8	1.585	1.595
(1) Fraction of hydrate (additional-water model)			*0.21*	*0.20*
(2) Fraction of hydrate (water-from-host model)			*0.10*	*0.09*
L70	1.960	3.8	1.675	1.690
(1) Fraction of hydrate (additional-water model)			*0.26*	*0.25*
(2) Fraction of hydrate (water-from-host model)			*0.14*	*0.12*
L100	1.980	3.8	1.680	1.700
(1) Fraction of hydrate (additional-water model)			*0.27*	*0.26*
(2) Fraction of hydrate (water-from-host model)			*0.14*	*0.13*

[a]Case 1, additional water model; case 2, water-from-host model. The estimations are done for the three layers presenting the highest Vp in the tomography model (L60, L70, L100). Hydrate concentration is given as a fraction of total volume, not as a fraction of pore space.

by blanking may indicate variation in the location and/or accumulation of gas hydrate [*Riedel et al.*, 2006]. Hence, we conjecture that seismic attenuation may come from discrete hydrate accumulations. If there is free gas in migration pathways of locally very high salinity, the amount is likely to be very small, and its effect on reducing Vp counteracted by the increased velocity produced by hydrate. The corollary of this is that if free gas is present, the estimates of hydrate content based on Vp will be too low.

6.2. Estimation of Gas Hydrate Concentration

[45] The increased seismic velocity at the chimney centre relative to that of the surrounding strata can be used to estimate the concentration of hydrate present. There are several published relationships between seismic properties and hydrate content in sediments, and most of them take into account the habit of the hydrate within the pores of the host sediment, such as pore-filling, frame-forming, cementing, and also in some cases the mineralogy of the host sediment [*Helgerud et al.*, 1999; *Lee et al.*, 1996; *Jakobsen et al.*, 2000; *Chand et al.*, 2004, 2006].

[46] All of them, however, assume that the hydrate occupies intergranular pore space, in one way or another. Hydrate found in cores at pockmarks 10 km from CNE03 [*Ivanov et al.*, 2007; *Akhmetzhanov et al.*, 2008] occupies bedding planes and fractures. Also, it has been observed that hydrate occupies networks with veins of a few centimeters separation in cores of fine-grained clay-rich mud sampled at in situ pressure from offshore India and South Korea [*Schultheiss et al.*, 2009]. Given the fine-grained, muddy character of the NAUST S and T units (layers L30–L100 in our model) [*Berg et al.*, 2005; *Rise et al.*, 2006], it is likely that hydrate in the chimney beneath CNE03 is predominantly fracture filling in its habit. Consequently, we have used a simple time-average approach to estimate the concentration of hydrate in the chimney. For each of the three layers of the model with significant lateral variation in velocity, L60, L70, and L100, we took the maximum velocity and compared it with maximum and minimum values of the background velocity of the layer in the well-constrained part of the model to derive estimates of the minimum and maximum proportion of sediment locally occupied by hydrate-filling veins, assuming

the background seismic velocity represented the velocity for hydrate-free sediment. This simple mixture model predicts more hydrate for a given velocity anomaly than frame-forming or cementing models for intergranular porosity but is comparable to pore-filling model predictions. We made hydrate-saturation estimates based on two different end-member assumptions:

[47] 1. Hydrate is an addition to the host sediment, so the mixture is between hydrate and unaltered host. This would be the case if hydrate formed from methane in solution, where both the methane and the water that form the hydrate are introduced to the GHSZ, displacing the sediment without changing the sediment's water content, porosity, or mechanical properties.

[48] 2. Only free gas is introduced into the veins, so the water to create hydrate in the veins must come from the pores of the host, reducing the water content and porosity of the host. In this case, one might assume that although the seismic velocity of the host is increased by the reduction in porosity, its matrix velocity is unaltered, but it appears unlikely that the host could compact beyond its elastic limit without an increase in its matrix velocity. Hence, we prefer a model in which the velocity of the host is increased by both the reduction in its porosity and the increase of its matrix velocity.

[49] Details of the derivations are given in Appendix C, and the results are shown in Table 2. Assumption (1) yields a higher hydrate saturation estimate than assumption (2) because the increase in the velocity of the host, as well as the presence of hydrate, contributes to the overall velocity increase, and so less hydrate is needed under assumption (2) to produce the velocity anomaly.

[50] In layer L100, the maximum velocity within the chimney is 1980 m/s, and the background velocity in the well-constrained part of the model varies between 1680 and 1700 m/s. This yields an estimate of maximum concentration of hydrate of 26%–27% of sediment volume with the (a) additional-water model and 13%–14% with the (b) water-from-host model. Layer L70 yields similar values, and layer L60 gives a range from 9% minimum with the (b) water-from-host model to 21% maximum with the (a) additional-water model. For comparison, if only the porosity changes

in the host for the water-from-host-model, the estimates of hydrate concentration (from equations C3 to C5 of Appendix C) are between 78% and 96% of those obtained with the (a) additional-water model. The increase in thickness of L100 where it achieves a maximum increase in velocity is only 20% greater than its normal thickness, whereas the (a) additional-water model predicts that it should be about 35% thicker if the hydrate occupies 26%–27% of the volume. For the water-from-host model, however, the maximum increase in volume in L100 is 2.7% (4.9% if the possible increase in host matrix velocity is ignored). Furthermore, layers L70 and L60 show no obvious thickening accompanying the increase in velocity in the core of the chimney. Consequently, we consider that the water-from-host model, with its lower predictions of hydrate concentration, is likely to represent the predominant mode of hydrate formation, although it is possible that, during the history of formation of the chimney, hydrate was also formed from methane in solution, giving the hydrate mixed modes of formation.

6.3. Processes and Time Scale for Formation of the Chimney

[51] To evaluate the possible occurrence of carbonate and gas hydrate in relation to the period of formation of the CNE03 chimney, we consider two scenarios: (1) the chimney grew over a long period of time, possibly with more than one period of activity (gas venting) and inactivity, and (2) the chimney is relatively young and developed rapidly during a single gas venting episode, probably at the end of the last glaciation (19–16 ka), during a period of fluid expulsion in this region suggested by *Hustoft et al.* [2009b].

6.3.1. Long-Period Formation Scenario

[52] In this scenario, the chimney has been active for hundreds of thousands of years and paleo-seepage features have been preserved through time within the structure of the chimney. As the base of the zone of high Vp lies near the base of the Naust S unit (Figure 9), the minimum period for the chimney's formation would be about 350,000 years [*Rise et al.*, 2006]. If the chimney has been active for about 350 ka without ceasing its activity completely, or if it had several long periods of activity during this time, we would expect to see some stratigraphic evidence such as onlap of reflectors against paleo-seabed mounds created during the active periods. However, there is no clear evidence for onlap of reflectors against the flanks of the CNE03 chimney (Figure 9) [*Westbrook et al.*, 2008b].

[53] In a long period of activity scenario, carbonate formed at shallow depth would extend through the stratigraphic range of sediment deposited during the period of the chimney's activity, and it is likely that carbonate would extend beneath the present GHSZ if the chimney had grown over a long period. No anomalous high-velocity material occurs beneath the chimney deeper than the present-day GHSZ (Figure 6).

[54] The lack of evidence for carbonate preservation between 80 and 250 mbsf, where the highest Vp anomaly occurs, and the lack of anomalously high Vp beneath the present GHSZ, make it unlikely that the chimney is 350 ka or older and has sustained activity over that period (Figure 10). On the basis of the data and other evidence available, we cannot, however, exclude the possibility of very intermittent,

short periods of activity, creating a few thin deposits of carbonate since 350 ka, the age of strata at the present-day base of the GHSZ.

6.3.2. Short-Period Formation Scenario

[55] In this scenario, formation of the CNE03 chimney began as a vigorous system with free gas entering the GHSZ. The beginning of the period over which chimney formation occurred and was most active is likely to be governed by external factors, such as rapid sediment loading in the latter stages of the last glacial leading to overpressured formations around 18 ka [*Hustoft et al.*, 2009b].

[56] From the general downward increase of anomalously high seismic velocity at CNE03 (Figures 6, 7, and 9), higher hydrate concentrations are predicted near the base of the GHSZ. This is consistent with formation of hydrate from the invasion of the GHSZ by free gas, comparable in its structure to the high-flux methane vent feature described by *Haacke et al.* [2009] offshore Korea. Gas invasion of the lower part of the GHSZ, probably in a series of periodic pulses to allow time for sufficient gas pressure to build up for each pulse, is the starting point for the model of chimney formation proposed by *Liu and Flemings* [2007], in which the upward migration of gas and the formation of hydrate is promoted by the increased salinity of pore water caused by the exclusion of ions from water when it forms hydrate. The model by *Liu and Flemings* [2007] provides a good basis for understanding how we believe the CNE03 chimney may have formed, with the qualification that the formation of fractures and fracture flow [*Jain and Juanes*, 2009] are likely to have played a more important role in the formation of CNE03 because the low permeability of the muddy-hemipelagic sediment of the Naust units [*Rise et al.*, 2006] is lower than those used in Liu and Flemings' models, which were for sand and silt. Consequently, a predominantly fracture-filling mode of hydrate emplacement appears most probable, although formation of hydrate locally in the intergranular pore space of permeable lithologies will also be expected.

[57] Later in the development of the chimney, such as at the present day, when there is very little or no flux of gaseous methane from the CNE03 pockmark, but evidence of methane seepage [*Nouzé and Fabri*, 2007] and shallow gas hydrate [*Akhmetzhanov et al.*, 2008], there can be continued formation of hydrate in the shallow part of the chimney from methane in solution carried upward by aqueous advection. This is supported by biochemical sampling at different localities within Nyegga. Carbonate at the G11 pockmark (south-west of CNE03) is associated with microseepage of light hydrocarbon [*Hovland et al.*, 2005]. Sampled pockmarks to the south–east of Nyegga [*Mazzini et al.*, 2005] and pockmarks located about 12 km west of CNE03 [*Paull et al.*, 2008], appeared to have ^{13}C depleted (decrease in ^{13}C molecules) and [18]O enriched (increase in [18]O molecules) authigenic carbonate. Positive values of [18]O indicate contribution of [18]O enriched water that may be related to gas hydrate dissociation [*Naehr et al.*, 2007].

[58] Advecting pore water saturated in methane can form hydrate throughout the depth range of the chimney because the solubility of methane in aqueous solution decreases with decreasing pressure [*Xu and Ruppel*, 1999; *Zatsepina and Buffet*, 1997] in the GHSZ. Undersaturated water entering the base of the chimney will become saturated by dissolving
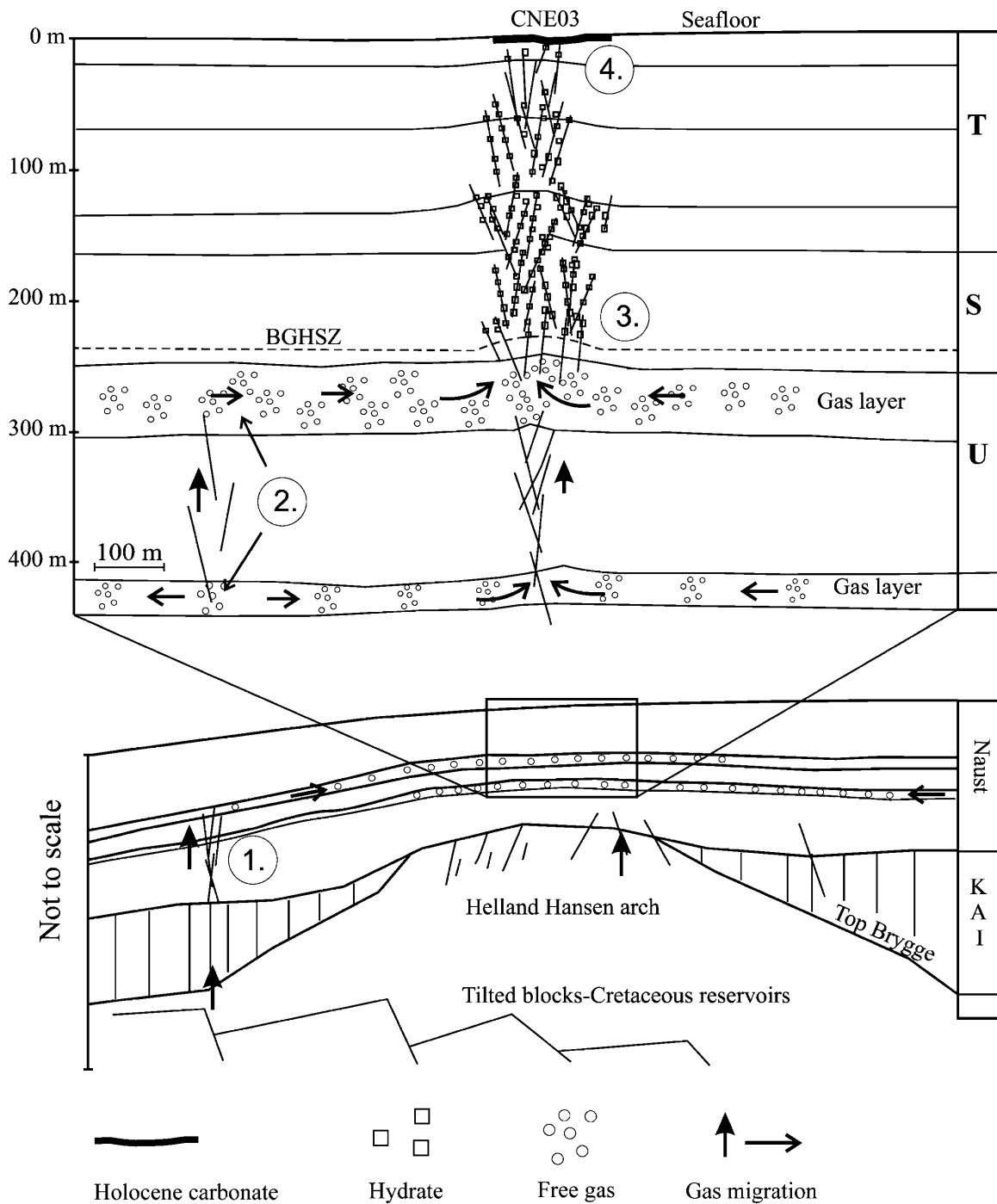
Figure 10. Schematic representation of the inferred internal structure and formation mechanism of the CNE03 chimney. In a short-period formation scenario, the chimney contains a fracture network where mainly gas hydrate is currently emplaced. The formation is explained in four steps involving migration of gas from deep sources and its passage through the GHSZ (see discussion). Two gas-rich layers supply the methane for hydrate formation inside the chimney. Doming of the strata seems to be related to hydrate accumulation. Carbonates form above the chimney at the seafloor and immediate sediments.

hydrate in the lowest part of the chimney and then form hydrate at shallower depths, effectively transporting hydrate from the deeper part of the chimney to the shallower part.

[59] The four stages we believe are important to the formation of the CNE03 chimney (Figure 10) can be summarized as follows:

[60] 1. Vertical migration of gas through polygonal faults and fractures from deep reservoirs [*Berndt et al.*, 2003; *Bünz et al.*, 2003; *Hustoft et al.*, 2007].

[61] 2. At a shallower level, gas migrates through the more permeable-porous units, accumulating in conventional stratigraphic and structural traps and at the base of the

GHSZ where it lies within permeable units, until it achieves a sufficient pressure to propagate fractures.

[62] 3. When the gas achieves a critical overpressure, it migrates rapidly into the GHSZ by creating fractures and forming hydrate in veins [*Hornbach et al.*, 2004; *Jain and Juanes*, 2009; *Liu and Flemings*, 2007] similar to those identified in pressure cores offshore India and Korea [*Schultheiss et al.*, 2009].

[63] 4. The input of gaseous methane decreases with time as a consequence of diminution of the process driving gas migration from deeper, but water with methane in solution continues to migrate upward, forming small amounts of hydrate throughout the GHSZ and authigenic carbonate close to the seafloor and supporting chemosynthetic biota [*Foucher et al.*, 2009]. This water is probably saturated in methane because the layer beneath the chimney contains free gas, but even if it is undersaturated, it will become saturated in methane by dissolving a proportion of the hydrate that it passes through in the lower part of the chimney.

[64] The contribution to the chimney formation from methane released by hydrate dissociation caused by post-glacial climate change is probably negligible or very minor because in the water depths greater than 700 m in this region, where the current seabed temperature is about −0.5°C [*Nouzé and Fabri*, 2007], the effect of sea level rise compensated the effect of seabed temperature increase upon the thickness of the GHSZ [e.g., *Mienert et al.*, 2005].

7. Conclusions

[65] A high-resolution seismic tomographic experiment has defined the main elements of the internal structure of a fluid-escape chimney and provided evidence for the presence of gas hydrate within it:

[66] 1. The core of the CNE03 chimney has a zone of anomalously high *P* wave velocity 500 m in diameter at its base and 200 m in diameter near the seabed that is restricted to the GHSZ. Vp increases laterally toward the center of the chimney. Beneath the GHSZ, the velocity distribution in each layer is homogenous with no major lateral changes in velocity.

[67] 2. The 230 m depth extent of the high-velocity zone and the absence of a high-velocity zone beneath the GHSZ, extending downward from the chimney, make it likely that the presence of hydrate is the primary cause of the high-velocity zone.

[68] 3. The seafloor and layers within the GHSZ are domed over the center of the chimney, in contrast to the planar strata surrounding and beneath the chimney. Stratal deformation beneath the GHSZ is minor. It appears that the emplacement of hydrate into veins and fractures has, in some way, created the up-doming, which is not inherited from a deeper structure.

[69] 4. We suggest a predominantly fracture-filling model is appropriate for the formation of hydrate in the fine-grained sediments in which the chimney occurs. The hydrate concentration calculated from anomalous Vp values is laterally and vertically heterogeneous. The highest hydrate concentration in the chimney is near the base of the GHSZ and may locally be as high as 27% of the total volume. However, it is likely that the maximum hydrate concentration is much less than 27% and may not exceed 14% of the total volume.

[70] We infer that the chimney is likely to have originated as a vigorous gas venting system that generated a fracture network in which hydrate formed, primarily in the lower part of the chimney. Two of the layers beneath the GHSZ, each of which have a *P* wave velocity that is less than that of the overlying unit and is laterally homogeneous, are inferred levels for local gas migration and accumulation. At present, with low rates of methane seepage methane in solution from the seabed, the chimney is likely to be dominated by the formation of hydrate from methane in aqueous solution. If the upwardly migrating pore water entering the base of the chimney is undersaturated in methane, dissolution of hydrate within the chimney will bring the methane in solution to saturation, some of which will be released to form hydrate at shallower depths where methane solubility is lower.

[71] The chimney has provided, through the formation of hydrate within it, a reservoir of methane that is apparently being released slowly at present, supporting chemosynthetic communities at the seabed and the formation of authigenic carbonate in the shallow sediment beneath. The creation of hydrate during the early stages of the chimney's formation, which will have reduced the amount of gas reaching the seabed, and hydrate dissolution within the chimney, which maintains a supply of methane to the surface when the input of methane from beneath the chimney has been reduced, act as a buffer on the supply of methane in solution to the seabed. If this is representative of this kind of chimney in general, it appears that chimneys have an important role in buffering, as well as enabling, the escape of methane from sources beneath the GHSZ.

Appendix A: Principle of Tomography Software

[72] Travel time tomography aims at determining the velocity model *m* that satisfies the travel times t^{obs} picked from the seismic data. This means that model *m* must satisfy

$$t^{obs} = t(m), \qquad (A1)$$

where *t* is the physical law that links the data space and the parameter space.

[73] As mentioned in section 4.2, the tomography software is based on a blocky velocity representation of the subsurface. The model *m* is thus made as follows:

$$m = \begin{pmatrix} \mathbf{v} \\ \mathbf{Z} \end{pmatrix}, \qquad (A2)$$

where **Z** is the vector containing the mathematical representation of each interface and vector **v** contains the mathematical representation of the velocity law of each velocity block. Since velocities are assumed vertically invariant within a layer for the model used for the CNE03 inversion, velocity laws for each block are limited to lateral velocity variations.

[74] The travel times supplied to the tomographic inversion are generally corrupted by errors, such as those from the finite frequency spectrum of seismic data, errors in temporal sampling, and interference of primary reflections with other seismic events (multiples, converted modes, surface waves, diffractions, etc). It is assumed that the travel

time errors have a Gaussian distribution, and a least-squares formulation is used to solve equation A1. Also, the inverse problem of travel time tomography is generally ill posed. Only a discrete number of traces are recorded, and the rays from which the travel times are taken may not have sampled reflectors regularly or continuously, and in any case, will have a limited incidence-angle range. To stabilize the inversion, a priori information about the expected model may be introduced and a regularized least-squares problem employed. As shown by *Delprat-Jannaud and Lailly* [1993], a priori information on the second derivatives of the model is necessary and sufficient to obtain a mathematically well-posed problem.

[75] Hence, the travel time tomography implementation that we used aims at determining the velocity model m that best satisfies the interpreted travel times t^{obs} and whose discrepancy with a priori model m^{prior} is characterized by a small roughness. Equation A1 is, therefore, reformulated as the minimization of the following cost function:

$$
\begin{aligned}
C(m) = & \sum_{i=1}^{NT} \sigma_i^{-2} \left(t_i(m) - t_i^{\text{obs}} \right)^2 \\
& + \sum_{i=1}^{NZ} \int_\Omega \varepsilon_{i,Z}^2(x,y) \left\| D^2 \left(Z^i(x,y) - \left(Z^i(x,y) \right)_{\text{prior}} \right) \right\|^2 \mathrm{d}x\mathrm{d}y \\
& + \sum_{i=1}^{NV} \int_\Omega \varepsilon_{i,v}^2(x,y) \left\| D^2 \left(v_0^i(x,y) - \left(v_0^i(x,y) \right)_{\text{prior}} \right) \right\|^2 \mathrm{d}x\mathrm{d}y,
\end{aligned}
$$

$$(A3)$$

where NT is the number of travel times, σ_i is the uncertainty of the observed travel times t_i^{obs} ($i = 1, \ldots, NT$), NZ is the number of interfaces of the model, $\varepsilon_{i,\mathbf{z}}$ is the regularization weight on the roughness of interface $\mathbf{Z}^i$ with respect to a priori interface $\mathbf{Z}_{\text{prior}}^i$ ($i = 1, \ldots, NZ$), NV is the number of lateral velocity laws, $\varepsilon_{i,v}$ is the regularization weight on the roughness of the lateral velocity law v_0^i with respect to a priori lateral velocity law $v_{0\text{prior}}^i$ ($i = 1, \ldots, NV$), $\| \; \|$ stands for the $\mathbf{L}^2$ norm, $\mathbf{D}^2$ is the total differential with respect to spatial coordinates of second order, and Ω is the model definition domain.

[76] Since the physical law t used to estimate calculated data for a given model m is nonlinear, the cost function described in equation A3 is nonquadratic. This nonlinear problem is solved iteratively with the Gauss-Newton method. For each iteration, the travel time function t is linearized around the current model. A model perturbation that minimizes the resulting quadratic cost function is computed (with a conjugate gradient algorithm) and used to update the current model. However, in some cases, the line search method is not able to ensure a satisfactory convergence. In order to improve the stability of the inversion process and accuracy of the inversion results, a "trust region" has been introduced [*Sebudandi and Toint*, 1993; *Delbos et al.*, 2001].

[77] Solving equation A3 requires defining regularization weights for each inverted lateral velocity law and each inverted interface. An inappropriate choice of those weights may have a strong impact on the solution of the inverse problem. Indeed if strong regularization weights are used, the regularization term will be predominant, and the solution model will not satisfy the travel time information sufficiently well. On the other hand, in case regularization weights that

are too small, the inversion problem will become ill conditioned and the inversion process will become unstable. To overcome those difficulties, tomography software implements an approach proposed by *Renard and Lailly* [1999]. This method consists of obtaining a first solution of the inverse problem by starting with strong regularization weights. Then, every p iteration of the Gauss-Newton process, the regularization weights are decreased, by dividing by a factor τ. This procedure is repeated until satisfactory travel time residuals are obtained that are not reduced further by lower regularization weights.

[78] In addition to classical regularization, information about the expected model may also be introduced as linear equality or inequality constraints. These constraints may correspond to geological or geophysical knowledge including well data, for example, by preventing nonphysical solutions and ensuring that interfaces do not cross each other. The constraints are generally used for managing expected velocity values or reflector depth, as well as their first-order and second-order derivatives (reflector dips, velocity gradients, reflector roughness, and velocity variations). The constraints can be applied globally or locally for a specific area. The least-square problem under constraints is solved by the optimization algorithm Sequential Quadratic Programming Augmented Lagrangian developed at IFP [*Delbos et al.*, 2006].

Appendix B: Analysis of Residuals and Model Assessment

B1. Residual Travel Times

[79] The distribution of travel time residuals and RMS values of residuals are used as a measure of the improvement in the travel times predicted by the models after each iteration. The residuals are presented at the location of the impact points (IPs) over each interface in the model (Figure B1). In general, the density of impact points is poor at the west half of the chimney.

[80] High positive travel time residuals ($T_{\text{calculated}} - T_{\text{observed}}$) indicate model velocities that are too low or thicknesses that are too great. Most of the residuals have values between -2 and 2 ms and are distributed around zero, indicating that the inversion has been optimized (Figure B2). The magnitudes of residuals are reduced to less than 2 ms at the flat parts of the layers. Slightly higher residuals (e.g., -5 and 5 ms) remain at the eastern flank within the upper 3 layers (Figure B1).

[81] The fact that high negative and high positive residuals are observed at the same location suggests that for OBSs recording at different sides of the chimney, the velocity is overestimated or underestimated depending on the direction of the raypaths. This may be related to the parameterization and regularization of the model (resolution of the experiment). Since the cell size is 40 m, velocities within 40 m (between two parameters in a layer) will be interpolated according to the regularization used for inversion. Impact points of rays with travel times recording passage through faster material might not be optimized if they are close to a parameter node where lower velocities (than the average velocity of their path) have been interpolated due to the dominancy of travel times of rays that do not pass through the faster material (Figure B3). On the other hand, travel times from rays with impact points close to parameter nodes with higher velocities may lead to over-
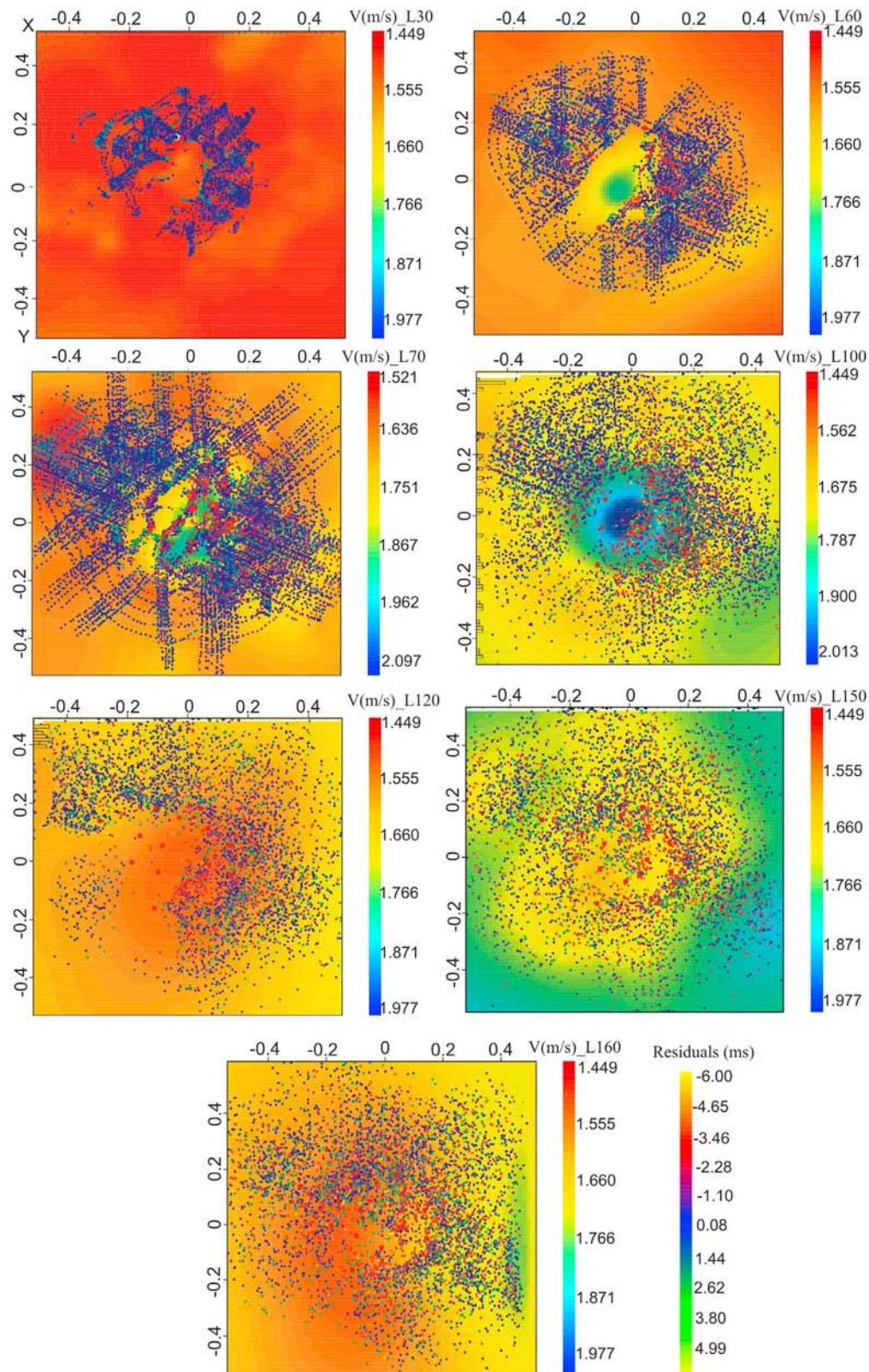
Figure B1. Residual distribution displayed at the locations of the impact points (IPs) for reflected arrivals recorded by OBS, shown in the top views of the velocity distribution for all the layers in the tomography model. A variable decimation factor (between 50 and 200, depending on the number of observed travel times at each layer) for the number of displayed IP, has been used to allow the visualization of the velocity model. *X* and *Y* scales are in kilometers. The velocity scales are in kilometers per second, and the residuals are in milliseconds.

Figure B2. Histograms with the residual distribution ($T_{\text{calculated}} - T_{\text{observed}}$) after tomographic inversion for each reflector in the model.

estimation of the velocity. At the depth of reflector H70 (~900 m), a 20 m/s velocity decrease/increase represents travel time differences of over 4 ms. This is consistent with the range of confidence that we find from synthetic modeling of H70.

[82] Residuals of reflectors H100–H160 appear less optimized (remaining residuals > ±6 ms) because of the uncertainties introduced by an incomplete modeling of interface H100. The uncertainties are inherited by deeper events. The RMS values increase from about 1 ms after inversion for the shallower reflectors to about 3 ms for the deeper ones (Table B1). The number of travel times from the seismic streamer data is between 9000 and 16,000 for all the layers. The number of OBS data travel times for each reflector included in the inversion is more variable. H70 and H100 have the highest number of observed travel times: 166,099 and 219,000, respectively. H60 and H120 have the lowest number of available observed data: 92,700 and 95,657, respectively (Table B1).

B2. Resolution and Uncertainty Tests

[83] In order to avoid misinterpretation of the structures appearing in the tomographic model, the lateral resolution of the velocity variations must be known [*Zelt*, 1998]. At the scale of our investigation, the velocity and interface depth do not show significant heterogeneity in flat and homogeneous parts of the model outside the chimney. Velocity values and interface depths are more heterogeneous inside the chimney and in the close vicinity of the chimney flanks. We have adapted the checkerboard test [*Leveque et al.*, 1993; *Schmelzbach et al.*, 2008; *Zelt*, 1998] to investigate the possible resolution that is allowed by the parameterization and regularization chosen for our model.

[84] Three checkerboards were created for layer L70 at 880 m depth (Figure B4), with square sizes of one cell (40 × 40 m), four cells (80 × 80 m), and nine cells (120 × 120 m). The velocity functions in the model for each square were alternately modified by plus or minus 5%, and the modified model was used to calculate synthetic travel times. These synthetic travel times were then tomographically inverted to
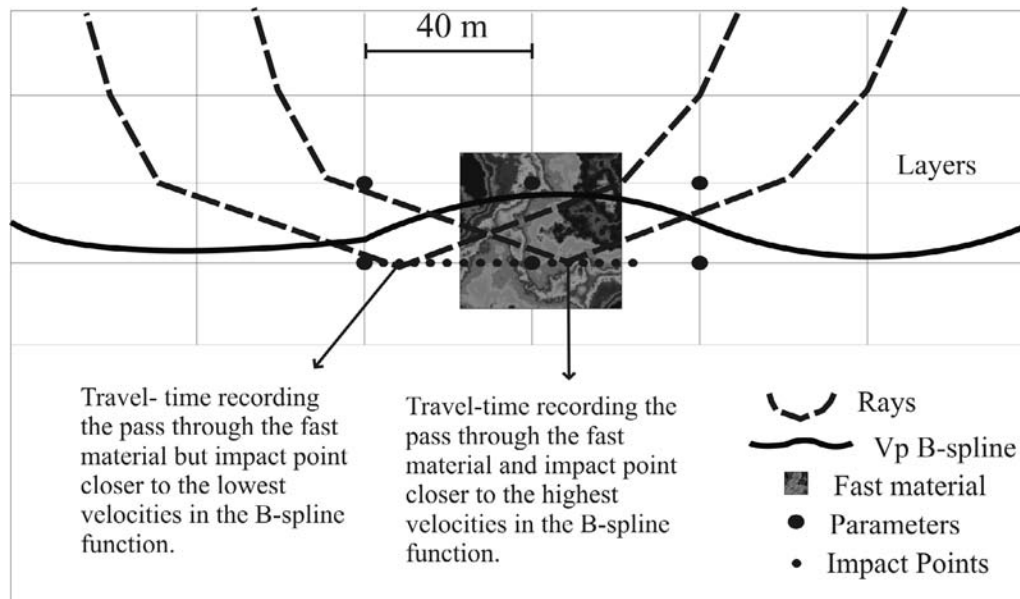
Figure B3. Diagram to show the relationship between the raypath and the location of its impact point respect to the minimum or maximum of the Vp B-spline function within cells.

test how well the checkerboard pattern in the modified model was retrieved.

[85] The checkerboard pattern at 120 m resolution is retrieved well, with differences between the retrieved and expected velocity of ±20 m/s (~1% of the velocities between 1500 and 2000 m/s) if a reliable number of travel times is available; areas with only a few impact points are still imaged but with velocity differences up to 50 m/s (Figure B4). The pattern with 80 m resolution (equivalent to four cells) is still resolved where there are sufficient travel times, with differences in velocity of 1%–2%. Where the number of travel times is low, the velocity differences can be up to 5% at this resolution (Figure B4). The pattern with a resolution of 40 m (one cell size) is barely retrieved. The B spline function does not accommodate the spatial frequency of velocity variation at 40 m.

[86] The effect of adding random noise with a 1 ms standard deviation to the synthetic data was evaluated for 80 and 120 m resolution at the depth of H70 (Figure B5). At 120 m resolution, seismically well-illuminated areas are not significantly affected. The velocities are retrieved with ~1.5% differences with respect to the expected velocities. At 80 m resolution, the match between expected and retrieved patterns is affected slightly, with differences up to 3% in well-illuminated areas, but the differences can be higher than 5% in areas with a poor impact point density (Figure B5). Testing with a different pseudorandom noise series, still with a 1 ms standard deviation, shows very similar results (Figure B5c). The effect of adding random noise is also shown in the magnitude of the misfit. Residuals, being all around zero in the synthetic inversion without noise, are up to ±3 ms after synthetic inversion of travel times with noise. The histogram showing the distribution of residuals (Figure B5d) is comparable with the histogram after inversion of H70 (Figure B2, H70).

[87] A second test evaluated the differences between the resulting and expected velocity and interface depth func-

tions without the effect of missing travel time picks, which reduce the illumination. A synthetic inversion was run for H70 with travel times for all the source-receiver pairs. The synthetic travel times were calculated from the resulting H70 model. The differences between the expected and resulting interface and velocity functions were less than 1 m and ±10 m/s, respectively, in the flat well-constrained areas (Figure B6). In a layer of ~30 m thickness with seismic velocities around 1800 m/s, these differences represent 3% of thickness and less than 1% of velocity. They increase to up to 1.4 m (5%) and 25 m/s (1.5%), respectively, at the center of the chimney where the interface is slightly more complex (relatively steep flanks and a relief of ~20 m) causing deviation of the rays and therefore decreasing the resolution in shadow areas. After the addition of random noise, the residuals are up to 4 ms, which is comparable to the misfit for our resulting H70 model (Figures B6c, B16f, B2, H70).

Appendix C: Calculation of Hydrate Concentration From Changes in *P* Wave Velocity

[88] In both cases used to estimate hydrate concentration, the hydrate is assumed to occupy fractures or veins cutting through the host sediment.

Table B1. List of RMS Values, Number of Ocean Bottom Seismometer Travel Times, and Number of Streamer Travel Times Used for Inversion of Each Layer in the Resulting Model

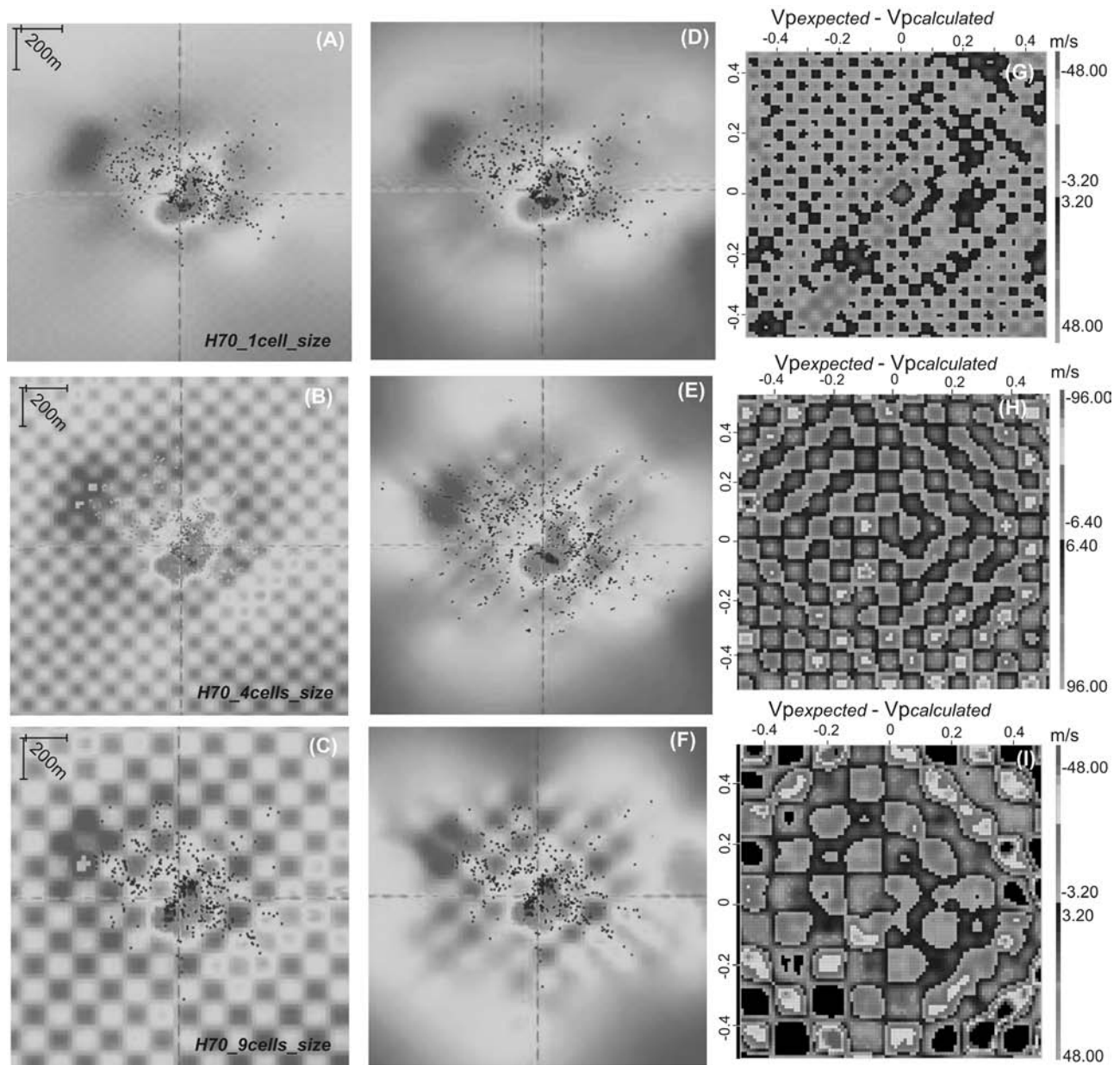| Layer	RMS (ms)	No. of OBS Rays	No. of Streamer Rays
L30	1.02	156,309	10,715
L60	1.06	92,700	15,912
L70	1.925	166,099	15,857
L100	2.275	219,000	14,820
L120	2.15	95,657	9709
L150	3.022	164,957	14,619
L160	2.947	123,909	12,576

Figure B4. Uncertainty test: checker board principle for reflector H70. Three Vp lateral perturbations were tried: (a) 40 (one cell size), (b) 80 (four cell size), and (c) 120 m (nine cell size). (d, e, and f) The calculated models are display next to the expected models for comparison. In Figures B4a–B4f, the dark and light color squares represent a Vp perturbation of +5% and −5%, respectively. (g, h, and i) The difference V_p expected − $V_p$calculated is illustrating the range of uncertainty (nonuniqueness) of the calculated models.

[89] 1. Hydrate is an addition to the host sediment, so the mixture is between hydrate and unaltered host. The velocity of the mixture is a time average between that of the host and that of hydrate, dependent on the fraction of the volume occupied by each.

$$1/v_{mix} = \phi_{hyd}/v_{hyd} + (1 - \phi_{hyd})/v_{host}, \qquad (C1)$$

where v_{hyd} is the acoustic velocity through hydrate, v_{host} is the velocity through the host sediment where it is unaffected

by hydrate formation, v_{mix} is the velocity through the mixture of host and hydrate in veins, and ϕ_{hyd} is the fraction of the mixture that is hydrate.

[90] Hence, the fraction occupied by hydrate filled veins,

$$\phi_{hyd} = (1/v_{mix} - 1/v_{host})/(1/v_{hyd} - 1/v_{host}). \qquad (C2)$$

[91] 2. If only free gas is introduced into the veins, the water to form hydrate must come from the pores of the host,
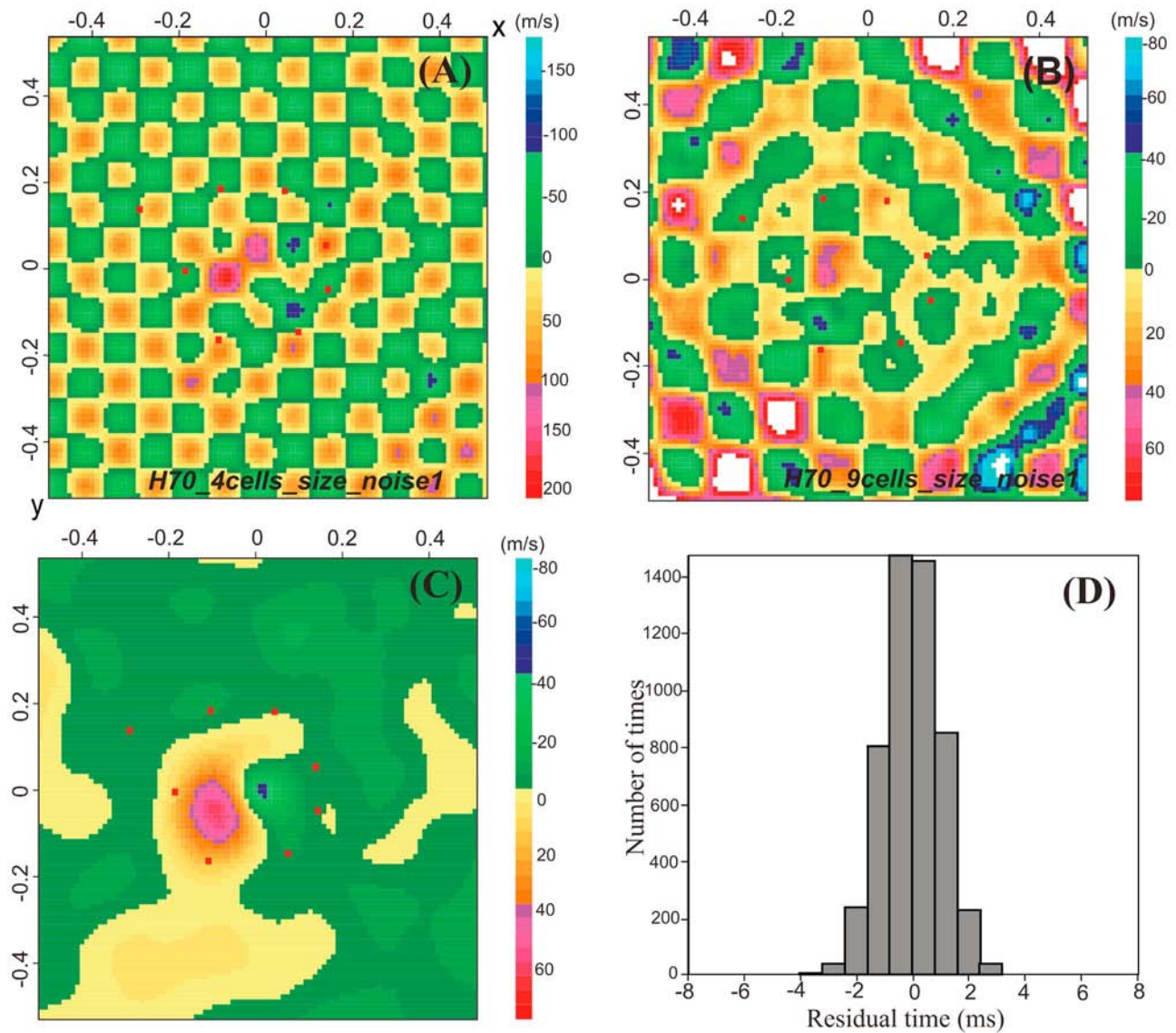
Figure B5. Top view of the velocity differences after synthetic modeling after addition of random noise for H70. Results for (a) four cell size and (b) nine cell size velocity perturbation are shown. The random noise has a Gaussian distribution of 1 ms standard deviation. (c) A second random distribution of the noise was tested for 4 cell size velocity perturbation. (d) The histogram of the residuals after synthetic inversion of noisy travel times can be compared with the histogram of the residuals of the resulting model (Figure B2, L70).

reducing the water content and porosity of the host. The velocity through the host is changed by the reduction in porosity caused by the withdrawal of pore water to create hydrate in the veins. If it is assumed that the velocity through the host matrix is unaltered, the time-average velocity of the mixture of hydrate-filled veins and the altered host sediment is given by

$$1/v_{mix} = (\phi_{hyd}/v_{hyd} + (\phi_i - f\phi_{hyd})/v_{water}$$
$$+ (1 - \phi_i)/v_{matrix})/(1 + (1 - f)\phi_{hyd}), \quad (C3)$$

where ϕ_i is the initial porosity of the host sediment, f is the fraction of a unit volume of water required to form a unit volume of hydrate and has the value 0.80 (assuming that water forms 87% of the mass of hydrate with a density of

920 kg/m^3), v_{water} is the velocity through pore water, and v_{matrix} is the velocity through the matrix of the host. The denominator in equation C3 normalizes the proportions in the mixture to account for the volume increase caused by the transformation of water into hydrate. Here v_{matrix} is derived by rearranging the time-average equation for the host with no hydrate present, $1/v_{host} = \phi_i/v_{water} + (1 - \phi_i)/v_{matrix}$. Hence,

$$v_{matrix} = (1 - \phi_i)/(1/v_{host} - \phi_i/v_{water}). \quad (C4)$$

So, by substituting the identity for v_{matrix} from (C4) into (C3) and rearranging terms,

$$\phi_{hyd} = (1/v_{mix} - 1/v_{host})/(1/v_{hyd} - f/v_{water} - (1 - f)/v_{mix}). \quad (C5)$$
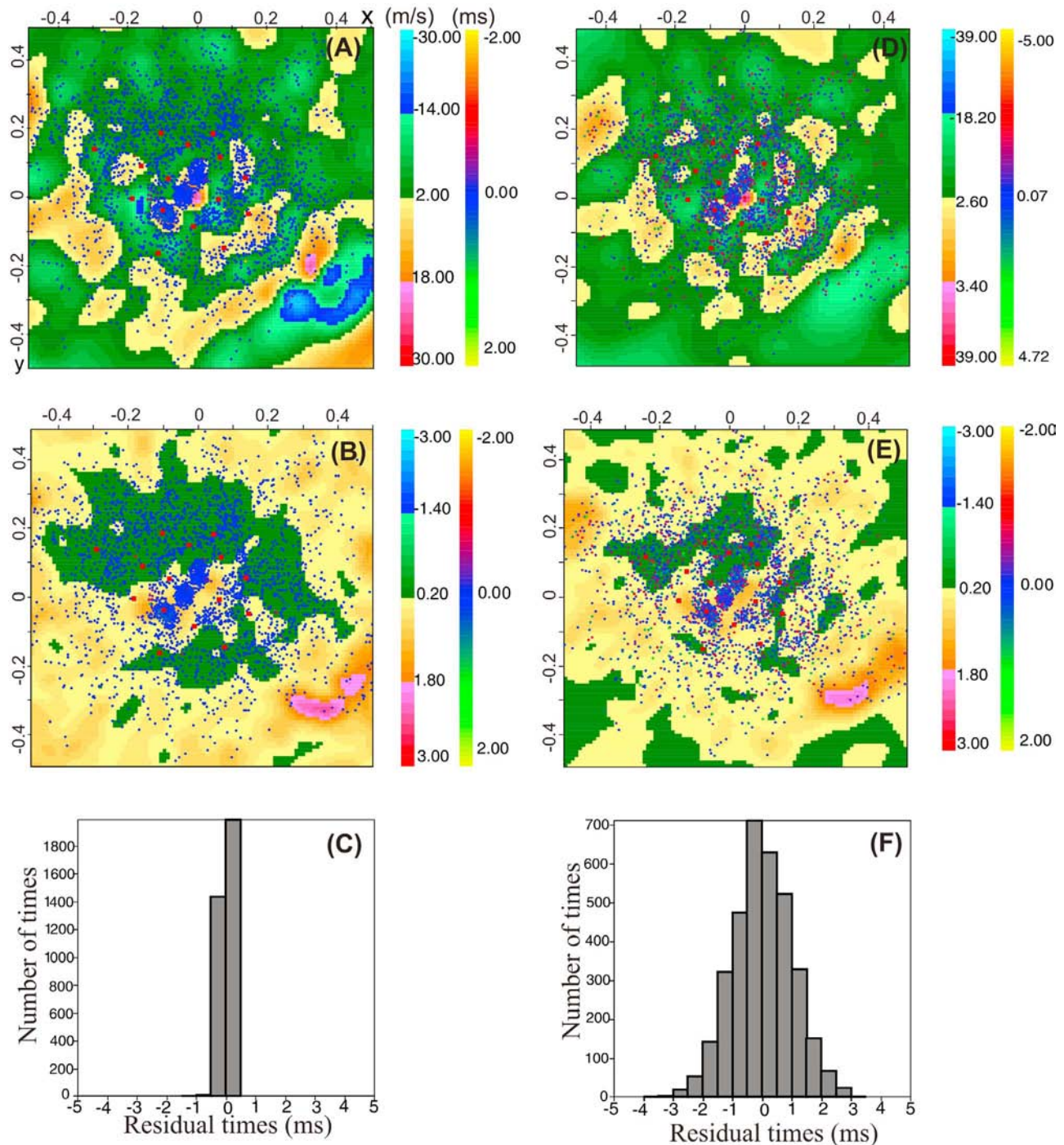
Figure B6. Uncertainty test 2: synthetic modeling completing the missing travel times for H70. (a and b) Top views show the velocity and interface depth differences after synthetic modeling. (d and e) The same random noise as for test 1 has been added to compare with the synthetics without noise. (c and f) Notice the changes in magnitude and distribution of the residuals after adding noise to the synthetic travel times by comparing histograms with and without noise.

It is not necessary to know the initial porosity of the host to estimate hydrate content. However, it is unlikely that the elastic moduli of the matrix are unaffected by the reduction in porosity and compaction resulting from water loss. To include the effect on the matrix velocity of a change in porosity in our estimate of the change in the velocity of the host, we use the velocity-density relationship for marine terrigenous sediment of *Hamilton* [1978], assuming a grain density of 2700 kg/m³.

[92] The initial porosity of the host is given by

$$\phi_i = (2890 - 1.135 v_{host})/1700, \qquad (C6)$$

with the velocity v_{host} given in meters per second.

[93] The altered velocity of the host is then

$$v_{\mathrm{mod}} = 2890/1.135 - 1700(\phi_{\mathrm{i}} - f\phi_{\mathrm{hyd}})/1.135, \qquad (C7)$$

with

$$\phi_{\mathrm{hyd}} = (1/v_{\mathrm{mix}} - 1/v_{\mathrm{mod}})/(1/v_{\mathrm{hyd}} - 1/v_{\mathrm{mod}}). \qquad (C8)$$

The fraction of volume filled by hydrate ϕ_{hyd} was solved iteratively by changing the value of ϕ_{hyd} in equation (C7) until it was within 10^{-7} of the value of ϕ_{hyd} yielded by equation (C8).

References

Akhmetzhanov, A. M., N. H. Kenyon, M. K. Ivanov, G. Westbrook, and A. Mazzini (2008), Deep-water depositional systems and cold seeps of the Western Mediterranean, Gulf of Cadiz and Norwegian continental margins, IOC Technical Series 76, UNESCO.

Berg, K., A. Solheim, and P. Bryn (2005), The Pleistocene to recent geological development of the Ormen Lange area, *Mar. Petrol. Geol.*, *22*(1–2), 45–56.

Berndt, C., S. Bunz, and J. Mienert (2003), Polygonal fault systems on the mid-Norwegian margin: a long-term source for fluid flow, *Subsurface Sediment Mobilization*, *216*, 283–290.

Bouriak, S., M. Vanneste, and A. Saoutkine (2000), Inferred gas hydrates and clay diapirs near the Storegga Slide on the southern edge of the Voring Plateau, offshore Norway, *Mar. Geol.*, *163*(1–4), 125–148.

Bouriak, S., A. Volkonskaia, and V. Galaktionov (2003), "Split" strata-bounded gas hydrate BSR below deposits of the Storegga Slide and at the southern edge of the Voring Plateau, *Mar. Geol.*, *195*(1–4), 301–318.

Brekke, H. (2000), The tectonic evolution of the Norwegian Sea Continental Margin with emphasis on the Voring and More Basins, in Dynamics of the Norwegian Margin, pp. 327–378, Geol. Soc. Publ. House, Bath, UK.

Broto, K., A. Ehinger, J. Kommedal, and P. Folstad (2003), Anisotropic traveltime tomography for depth consistent imaging of PP and PS data, *Leading Edge*, February.

Bünz, S., and J. Mienert (2004), Acoustic imaging of gas hydrate and free gas at the Storegga Slide, *J. Geophys. Res.*, *109*, B04102, doi:10.1029/2003JB002863.

Bünz, S., J. Mienert, and C. Berndt (2003), Geological controls on the Storegga gas hydrate system of the mid-Norwegian continental margin, *Earth Planet. Sci. Lett.*, *209*(3–4), 291–307.

Bünz, S., J. Mienert, M. Vanneste, and K. Andreassen (2005), Gas hydrates at the Storegga Slide: Constraints from an analysis of multicomponent, wide-angle seismic data, *Geophysics*, *70*(5), B19–B34.

Chand, S., T. A Minshull, D. Gei, and J. M Carcione (2004), Elastic velocity models for gas hydrate-bearing sediments: A comparison, *Geophys. J. Int.*, *159*(2), 573–590.

Chand, S., T. A. Minshull, J. A. Priest, A. I. Best, C. R. I. Clayton, and W. F. Waite (2006), An effective medium inversion algorithm for gas hydrate quantification and its application to laboratory and borehole mea-

surements of gas hydrate-bearing sediments, *Geophys. J. Int.*, *166*(2), 543–552.

Chand, S., L. Rise, D. Ottesen, M. F. J. Dolan, V. Bellec, and R. Boe (2009), Pockmark-like depressions near the Goliat hydrocarbon field, Barents Sea: Morphology and genesis, *Mar. Petrol. Geol.*, *26*(7), 1035–1042.

Clarke, R. A. (1996), Ray tracing and tomography friendly geological model, KIM 1996 Annual Report, Institut Français du Pétrole, Pau, France. (http://consortium.ifp.fr/KIM/)

Delbos, F., D. Sinoquet, J. Ch. Gilbert, and R. Masson (2001), Trust-region Gauss-Newton method for reflection tomography, KIM 2001 Annual Report, Institut Français du Pétrole, Rueil, France.

Delbos, F., J. C. Gilbert, R. Glowinski, and D. Sinoquet (2006), Constrained optimization in reflection tomography: an Gauss-Newton augmented Lagrangian method, *Geophys. J. Int.*, *164*, 670–684.

Delprat-Jannaud, F., and P. Lailly (1993), Ill-posed and well-posed formulations of the reflection travel time tomography problem, *J. Geophys. Res.*, *98*, 6589–6605.

Foucher, J. P., G. K. Westbrook, A. Boetius, S. Ceramicola, S. Dupre, J. Mascle, J. Mienert, O. Pfannkuche, C. Pierre, and D. Praeg (2009), Structure and Drivers of Cold Seep Ecosystems, *Oceanography*, *22*(1), 92–109.

Ehinger, A., K. Broto, and A. Jardin (2001) 3D tomographic velocity model determination for two North Sea case studies, 63rd Ann. Internat. Mtg., EAGE, Expanded Abstract.

Gómez, M., and J. Vergés (2005), Quantifying the contribution of tectonics vs. differential compaction in the development of domes along the mid-Norwegian Atlantic margin, *Basin Res.*, *17*(2), 289–310.

Hamilton, E. L. (1978), Sound velocity-density relations in sea floor sediments and rocks, *J. Acoust. Soc. Am.*, *63*, 366.

Helgerud, M. B., J. Dvorkin, A. Nur, A. Sakai, and T. Collett (1999), Elastic-wave velocity in marine sediments with gas hydrates: Effective medium modeling, *Geophys. Res. Lett.*, *26*(13), 2021–2024.

Hjelstuen, B. O., O. Eldholm, and J. Skogseid (1999), Cenozoic evolution of the northern Voring margin, *Geol. Soc. Am. Bull.*, *111*(12), 1792–1807.

Hjelstuen, B. O., H. P. Sejrup, H. Haflidason, A. Nygard, S. Ceramicola, and P. Bryn (2005), Late Cenozoic glacial history and evolution of the Storegga Slide area and adjacent slide flank regions, Norwegian continental margin, *Mar. Petrol. Geol.*, *22*(1–2), 57–69.

Hornbach, M. J., D. M. Saffer, and W. S. Holbrook (2004), Critically pressured free-gas reservoirs below gas hydrate provinces, *Nature*, *427*(6970), 142–144.

Hovland, M., and H. Svensen (2006), Submarine pingoes: Indicators of shallow gas hydrates in a pockmark at Nyegga, Norwegian Sea, *Mar. Geol.*, *228*(1–4), 15–23.

Hovland, M., H. Svensen, C. F. Forsberg, H. Johansen, C. Fichler, J. H. Fossa, R. Jonsson, and H. Rueslatten (2005), Complex pockmarks with carbonate-ridges off mid-Norway: Products of sediment degassing, *Mar. Geol.*, *218*(1–4), 191–206.

Hustoft, S., S. Bünz, J. Mienert, and S. Chand (2009a), Gas hydrate reservoir and active methane-venting province in sediments on < 20 Ma young oceanic crust in the Fram Strait, offshore NW-Svalbard, *Earth Planet. Sci. Lett.*, *284*(1–2), 12–24.

Hustoft, S., B. Dugan, and J. Mienert (2009b), Effects of rapid sedimentation on developing the Nyegga pockmark field: Constraints from hydrological modeling and 3-D seismic data, offshore mid-Norway, *Geochem. Geophys. Geosyst.*, *10*, Q06012, doi:10.1029/2009GC002409.

Hustoft, S., J. Mienert, S. Bünz, and H. Nouzé (2007), High-resolution 3-D seismic data indicate focused fluid migration pathways above polygonal fault systems of the mid-Norwegian margin, *Mar. Geol.*, *245*, 89–106.

Haacke, R. R., R. D. Hyndman, K. P. Park, D. G. Yoo, I. Stoian, and U. Schmidt (2009), Migration and venting of deep gases into the ocean through hydrate-choked chimneys offshore Korea, *Geology*, *37*(6), 531–534.

Ivanov, M., G. K. Westbrook, V. Blinova, E. Kozlova, A. Mazzini, H. Nouzé, and T.A. Minshull (2007), First sampling of gas hydrate from the Vøring Plateau, *Eos Trans. AGU*, *88*(19), 209.

Jain, A. K., and R. Juanes (2009), Preferential Mode of gas invasion in sediments: Grain-scale mechanistic model of coupled multiphase fluid flow and sediment mechanics, *J. Geophys. Res.*, *114*, B08101, doi:10.1029/2008JB006002.

Jakobsen, M., J. A. Hudson, T. A. Minshull, and S. C. Singh (2000), Elastic properties of hydrate-bearing sediments using effective medium theory, *J. Geophys. Res.*, *105*(B1), 561–577.

Jardin, A., M. Bêche, K. Broto, D. Saucier, and D. Kirkwood (2006), Combining geology and seismic travel-time inversion for structural model building in the Gaspé belt (Québec, Canada), CSEG/CSPG/CWLS convention, Calgary.

Jose, T., T. A. Minshull, G. K. Westbrook, H. Nouzé, S. Ker, A. Gailler, R. Exley, and C. Berndt (2008), A Geophysical Study of a Pockmark in the Nyegga Region, Norwegian Sea, in *Proceedings of the 6th International Conference on Gas Hydrates (ICGH 2008)*, 12 pp. Vancouver, BC, Canada, July 6–10. (https://circle.ubc.ca/handle/2429/1022)

Jurado, F., D. Sinoquet, and P. Lailly (1996) Jerry: a 3D reflection tomography designed for complex structures, *KIM 1996 Annu. Rep.*, IFP, Pau, France. (Available at http://consortium.ifp.fr/KIM/KIM_BIBLIOGRAPHY/Jurado/jerry.pdf)

Kvenvolden, K. A. (2002), Methane hydrate in the global organic carbon cycle, *Terra Nova*, *14*(5), 302–306.

King, L. H., and B. MacLean (1970), Pockmarks on the Scotian shelf, *Bull. Geol. Soc. Am.*, *81*(10), 3141–3148.

Kjeldstad, A., J. Skogseid, H. P. Langtangen, K. Bjorlykke, and K. Hoeg (2003), Differential loading by prograding sedimentary wedges on continental margins: An arch-forming mechanism, *J. Geophys. Res.*, *108*(B1), 2036, doi:10.1029/2001JB001145.

Lailly, P., and D. Sinoquet (1996), Smooth velocity models in reflection tomography for imaging complex geological structures, *Geophys. J. Int.*, *124*(2), 349–362.

Lee, M. W., D. R. Hutchinson, T. S. Collett, and W. P. Dillon (1996), Seismic velocities for hydrate-bearing sediments using weighted equation, *J. Geophys. Res.*, *101*(B9), 20,347–20,358.

Leveque, J. J., L. Rivera, and G. Wittlinger (1993), On the use of the checkerboard test to assess the resolution of tomographic inversions, *Geophys. J. Int.*, *115*(1), 313–318.

Liu, X. L., and P. B. Flemings (2007), Dynamic multiphase flow model of hydrate formation in marine sediments, *J. Geophys. Res.*, *112*, B03101, doi:10.1029/2005JB004227.

Mazzini, A., G. Aloisi, G.G. Akhmanov, J. Parnell, B.T. Cronin, and P. Murphy (2005), Integrated petrographic and geochemical record of hydrocarbon seepage on the Vøring Plateau, *J. Geol. Soc.*, *162*, 815–827.

Mazzini, A., H. Svensen, M. Hovland, and S. Planke (2006), Comparison and implications from strikingly different authigenic carbonates in a Nyegga complex pockmark, G11, Norwegian Sea, *Mar. Geol.*, *231*(1–4), 89–102.

Mienert, J., J. Posewang, and M. Baumann (1998), Gas hydrates along the north-eastern Atlantic Margin: possible hydrate bound margin instabilities and possible release of methane, in *Gas Hydrates: Relevance to World Margin Stability and Climatic Change*, edited by J.-P. Henriet, and J. Mienert, *Geol. Soc. London, Spec. Publ.*, *137*, 275–291.

Mienert, J., M. Vanneste, S. Bünz, K. Andreassen, H. Haflidason, and H. P. Sejrup (2005), Ocean warming and gas hydrate stability on the mid-Norwegian margin at the Storegga Slide, *Mar. Petrol. Geol.*, *22*(1–2), 233–244.

McIver, R. D. (1982), Role of naturally occurring gas hydrates in sediment transport, *AAPG Bull*, *66*, 789–792.

Naehr, T. H., P. Eichhubl, V. J. Orphan, M. Hovland, C. K. Paull, W. Ussler, T. D. Lorenson, and H. G. Greene (2007), Authigenic carbonate formation at hydrocarbon seeps in continental margin sediments: A comparative study, *Deep Sea Res. Part II*, *54*, 1268–1291.

Nouzé, H., and M.-C. Fabri (2007), Vicking cruise report: Cold seeps on the Norwegian Margin. Associated ecosystem: R/V Pourquoi pas? 19 May to 18 June 2006. Alesund- Alesund. Report GM/07- 02, Ifremer, Département des Géosciences Marines, Ifremer.

Paull, C. K., W. Ussler, W. S. Holbrook, T. M. Hill, R. Keaten, J. Mienert, H. Haflidason, J. E. Johnson, W. J. Winters, and T. D. Lorenson (2008), Origin of pockmarks and chimney structures on the flanks of the Storegga Slide, offshore Norway, *Geo-Mar. Lett.*, *28*(1), 43–51.

Plaza-Faverola, A., S. Bünz, and J. Mienert (2010), Fluid distributions inferred from P-wave velocity and reflection seismic amplitude anomalies beneath the Nyegga pockmark field of the mid-Norwegian margin, *Mar. Petrol. Geol.*, *27*(1), 46–60.

Reemst, P., J. Skogseid, and B. T. Larsen (1996), Base Pliocene velocity inversion on the eastern Voring Margin - Causes and implications, *Global Planet. Change*, *12*(1–4), 201–211.

Renard, F., and P. Lailly (1999), Robust and accurate determination of complex velocity/depth models by reflection travel time tomography: KIM 1999 Annual Report, Institut Français du Pétrole, Rueil-Malmaison, France. (http://consortium.ifp.fr/KIM/)

Riedel, M., I. Novosel, G. D. Spence, R. D. Hyndman, R. N. Chapman, R. C. Solem, and T. Lewis (2006), Geophysical and geochemical signatures associated with gas hydrate-related venting in the northern Cascadia margin, *Geol. Soc. Am. Bull.*, *118*(1–2), 23–38.

Rise, L., D. Ottesen, O. Longva, A. Solheim, E. S. Andersen, and S. Ayers (2006), The Sklinnadjupet slide and its relation to the Elsterian glaciation on the mid-Norwegian margin, *Mar. Petrol. Geol.*, *23*(5), 569–583.

Schmelzbach, C., C. A. Zelt, C. Juhlin, and R. Carbonell (2008), P- and S-V-velocity structure of the South Portuguese Zone fold-and-thrust belt, SW Iberia, from traveltime tomography, *Geophys. J. Int.*, *175*(2), 689–712.

Schultheiss, P., M. Holland, and G. Humphrey (2009), Wireline coring and analysis under pressure: Recent use and future developments of the HYACINTH System. Scientific Drilling, 7, March 09, 44–50, doi:10.2204/iodp.sd.7.07.2009.

Sebudandi, C., and P. L. Toint (1993), Nonlinear optimization for seismic travel time tomography, *Geophys. J. Int.*, *115*, 929–940.

Sundvor, E., O. Eldholm, T. P. Gladczenko, and S. Planke (2000), Norwegian-Greenland Sea thermal field, in *Dynamics of the Norwegian Margin Geological Society of London, Special Publication*, edited by A. Nøttvedt, 397–410.

Vogt, P. R., K. Crane, E. Sundvor, M. D. Max, and S. L. Pfirman (1994), Methane-generated (?) pockmarks on young, thickly sedimented oceanic-crust in the Arctic: Vestnesa Ridge, Fram strait, *Geology*, *22*(3), 255–258.

Westbrook, G. K., et al. (2008a), Estimation of gas hydrate concentration from multi-component seismic data at sites on the continental margins of NW Svalbard and the Storegga region of Norway, *Mar. Petrol. Geol.*, *25*(8), 744–758.

Westbrook, G. K., R. Exley, T. A. Minshull, H. Nouzé, A. Gailler, T. Jose, S. Ker, and A. Plaza (2008b), High-resolution 3-D seismic investigations of hydrate-bearing fluid-escape chimneys in the Nyegga region of the Vøring plateau, Norway, in *Proceedings of the 6th International Conference on Gas Hydrates (ICGH 2008)*, Vancouver, BC, Canada, July 6–10, 12 pp. (https://circle.ubc.ca/handle/2429/1022)

Xu, W., and C. Ruppel (1999), Predicting the occurrence, distribution, and evolution of methane gas hydrate in porous marine sediments, *J. Geophys. Res.*, *104*(B3), 5081–5095, doi:10.1029/1998JB900092.

Zatsepina, O. Y., and B. A. Buffett (1997), Phase equilibrium of gas hydrate: implications for the formation of hydrate in the deep sea floor, *Geophys. Res. Lett.*, *24*(13), 1567–1570, doi:10.1029/97GL01599.

Zelt, C. A. (1998), Lateral velocity resolution from three-dimensional seismic refraction data, *Geophys. J. Int.*, *135*(3), 1101–1112.

K. Broto, Institut Français du Pétrole, 1 & 4, avenue de Bois-Préau, 92852 Rüeil-Malmaison, France.

R. J. K. Exley and G. K. Westbrook, School of Geography, Earth & Environmental Sciences, University of Birmingham, Edgbaston, Birmingham B15 2TT, UK.

A. Gailler, Institut Universitaire Européen de la Mer, IUEM Technopole Brest-Iroise, rue Dumont d'Urville, 29280 Plouzané, France.

S. Ker, Département Géosciences Marines, Ifremer, Z.I Pointe du Diable, 29280 Plouzané, France.

T. A. Minshull, University of Southampton, National Oceanography Centre, Southampton European Way, Southampton SO14 3ZH, UK.

A. Plaza-Faverola, Department of Geology, University of Tromsø, Dramsveien 201, N-9037 Tromsø, Norway. (andreia.a.faverola@uit.no)